Membrane-mediated fibrillation and toxicity of the tau hexapeptide PHF6

Received for publication, July 1, 2019, and in revised form, August 18, 2019 Published, Papers in Press, August 22, 2019, DOI 10.1074/jbc.RA119.010003

Adeline M. Fanni[‡§1], Crystal M. Vander Zanden[‡¶1], Paulina V. Majewska[‡], Jaroslaw Majewski[¶‖], and Eva Y. Chi[‡¶2]**

*From the [‡]Center for Biomedical Engineering, [§]Biomedical Engineering Graduate Program, and [¶]Department of Chemical and Biological Engineering, University of New Mexico, Albuquerque, New Mexico 87131, the [‖]Department of Theoretical Biology and Biophysics, Los Alamos National Laboratory, Los Alamos, New Mexico 87545, and the **Division of Molecular and Cellular Biosciences, National Science Foundation, Alexandria, Virginia 22314*

Edited by Wolfgang Peti

The aggregation of the tau protein into neurofibrillary tangles is believed to correlate with cognitive decline in several neurodegenerative disorders, including Alzheimer's disease. Recent studies suggest that tau's interactions with the cell membrane could serve as a toxicity pathway and also enhance fibrillation into paired helical filaments (PHFs). Conformational changes associated with tau-membrane interactions are poorly understood, and their characterization could improve our understanding of tau pathogenicity. In this study, we investigated the molecular level structural changes associated with the interaction of the tau hexapeptide PHF6 with model lipid membranes and characterized the effects of these interactions on membrane stability and peptide fibrillation. We used two PHF6 forms, the aggregation-prone PHF6 with N-terminal acetylation (Ac-PHF6) and the non-aggregation prone PHF6 with a standard N terminus (NH_3^+-PHF6). We found that both PHF6 peptides are neurotoxic and exhibit similar membrane-mediated changes, consisting of: 1) favorable interactions with anionic membranes, 2) membrane destabilization through lipid extraction, and 3) membrane-mediated fibrillation. The rate at which these changes occurred was the main difference between the two peptides. NH_3^+-PHF6 displayed slow membrane-mediated fibrillation after 6 days of incubation, whereas Ac-PHF6 adopted a β-sheet conformation at the surface of the membrane within hours. Ac-PHF6 interactions with the membrane were also accompanied by membrane invagination and rapid membrane destabilization. Overall, our results reveal that membrane interactions could play a critical role in tau toxicity and fibrillation, and highlight that unraveling these interactions is important for significantly advancing the development of therapeutic strategies to manage tau-associated neurodegenerative diseases.

The misfolding and aggregation of the microtubule-associated protein tau into neurofibrillary tangles (NFTs)[3] is implicated in the development of Alzheimer's disease (AD) and other tauopathies such as Down's syndrome and frontotemporal dementia (1). The tau protein is composed of a projection domain made of acidic and proline-rich regions and a microtubule-binding (MTB) domain containing up to four repeat units made of tubulin-binding motifs (Fig. 1) (2, 3). The physiological function of tau is to stabilize microtubules (4, 5) to ensure cytoskeletal organization and cellular trafficking (6). Tau's function is modulated by post-translational modifications such as phosphorylation, which controls its affinity to the microtubules (7, 8). In AD, tau is hyperphosphorylated, which leads to the abnormal accumulation of unattached tau and promotes self-aggregation into insoluble paired helical filaments (PHFs) (6). The deposition of NFTs was found to correlate with cognitive decline and neurodegeneration (9), and is involved in the rapid transcellular propagation of the disease (10).

The MTB domain plays major roles in both tau's physiological function and aggregation. Indeed, the MTB domain forms the core of PHFs. In particular, two hexapeptide segments, ^{275}VQIINK^{280} (PHF6*) and ^{306}VQIVYK^{311} (PHF6) located in the second and third repeat units of the MTB domain, respectively, have been identified as aggregation promoting β-sheet forming motifs (11–13). Both hexapeptides form stable parallel β-sheet–twisted filaments similar to the β-sheet structures found in tau-oligomers and NFTs (14, 15), which make them

This work was supported by National Science Foundation Grants 1150855 and 1605225 (to E. Y. C.), National Institutes of Health Grant NIGMS 5K12GM088021-09 (to C. M. V. Z.), and Independent Research and Development program grant from the National Science Foundation (to J. M.). The authors declare that they have no conflicts of interest with the contents of this article. The content is solely the responsibility of the authors and does not necessarily represent the official views of the National Institutes of Health.

This article contains "Experimental procedures," Figs. S1–S5, and Tables S1–S4.

[1] Both authors have contributed equally to this article.

[2] To whom correspondence should be addressed: Dept. of Chemical and Biological Engineering, University of New Mexico, Albuquerque, NM 87131. Tel.: 505-277-2263; E-mail: evachi@unm.edu.

[3] The abbreviations used are: NFTs, neurofibrillary tangles; Ac-PHF6, N-terminal acetylated PHF6; AD, Alzheimer's disease; DLS, dynamic light scattering; DMPG, 1,2-dimyristoyl-*sn*-glycero-3-phosphorylglycerol; EthD-1, ethidium homodimer-1; FM, fluorescence microscopy; GIXD, grazing incidence X-ray diffraction; LC, liquid condensed; LE, liquid expanded; LUV, large unilamellar vesicles; MTB, microtubule binding; MTS, 3-(4,5-dimethyl-2-yl)-5-(3-carboxymethoxyphenyl)-2-(4-sulfophenyl)-2*H*-tetrazolium; NH_3^+-PHF6, PHF6 with a standard N-terminus; PHF, paired helical filaments; POPC, 1-palmitoyl-2-oleoyl-*sn*-glycero-3-phosphocholine; POPG, 1-palmitoyl-2-oleoyl-*sn*-glycero-3-phospho-(1′-*rac*-glycerol); TEM, transmission electron microscopy; TR-DHPE, Texas Red 1,2-dihexadecanoyl-*sn*-glycero-3-phosphoethanoloamine triethylammonium salt; XR, X-ray reflectivity; DMEM, Dulbecco's modified Eagle's medium; FBS, fetal bovine serum; TRITC, tetramethylrhodamine isothiocyanate.

Published in the U.S.A.

Downloaded from http://www.jbc.org/ at ARGONNE NATIONAL LABORATORY on January 13, 2020

relevant models of the full-length tau to investigate tau aggregation pathways (16).

Tau's toxicity mechanism is not well-understood. However, recent studies indicate that tau binding to the lipid membrane disrupts cell membrane homeostasis and causes apoptosis (17, 18). There are several hypothesized mechanisms by which amyloid proteins interact with and destabilize lipid membranes. Amyloid-β (Aβ), α-synuclein and amylin proteins have been described to form "ion-channel-like structures" on the cell membrane (19), which permeates the membrane and allows calcium flux (20). Aβ and α-synuclein have also been shown to remodel lipid membranes through a "carpeting-effect mechanism" (21), wherein the amyloid proteins blanket the lipid membrane causing membrane thinning (22) or generating membrane curvature (23, 24). Membrane disruption can also be caused by a "detergent-like mechanism" as observed with Aβ (21), where the peptide removes lipids from the membrane by forming micelle-like structures with the lipids. Tau protein was also shown to extract lipids through a similar mechanism leading to the formation of stable protein-lipid complexes (17). Molecular level details of lipid membrane destabilization caused by tau protein, however, remain poorly understood.

Tau interaction with the cell membrane is also suspected to nucleate fibrillation. Previous studies have shown that upon interaction with anionic lipid membrane, tau (25, 26), Aβ (27), and α-synuclein (28, 29) are more prone to fibril formation. Possible explanations for accelerated fibril nucleation include membrane-induced changes to protein structure, partial folding of the intrinsically disordered proteins via membrane association or penetration, and increased protein concentration at the membrane (30). In tau protein, three segments located in the MTB domain (253–261, 315–323, and 346–355) have been found to bind to lipid membranes and adopt a helical structure that promotes protein aggregation by enhancing protein-protein interactions (18, 31).

In this study, the hexapeptide PHF6 was used as a model tau protein because of its importance in promoting tau aggregation, and the peptide on its own has been shown to recapitulate important fibril forming and toxic properties of the full-length tau (14, 15). Truncated tau constructs, for example, K18, K19, and K32, have been routinely used as model tau proteins to investigate tau aggregation and pathological properties. Thus, insights gained about the membrane interaction, fibrillation, and toxicity of the PHF6 peptide will enhance our understanding of tau's role in neurodegenerative diseases and could lead to significant advancement in the development of therapeutic strategies to manage tau-associated neurodegenerative diseases.

We investigated the molecular level structural changes associated with the insertion of two PHF6 isoforms into lipid membranes and explored the effects on membrane stability and peptide fibrillation. After characterizing fibrillation of both peptides, their neuronal cell toxicity was evaluated. Angstrom level structural changes associated with PHF6 insertion into a lipid monolayer membrane at the air/water interface were investigated by *in situ* synchrotron X-ray reflectivity (XR) and grazing incidence X-ray diffraction (GIXD). The membrane-mediated conformational changes and fibrillation of PHF6

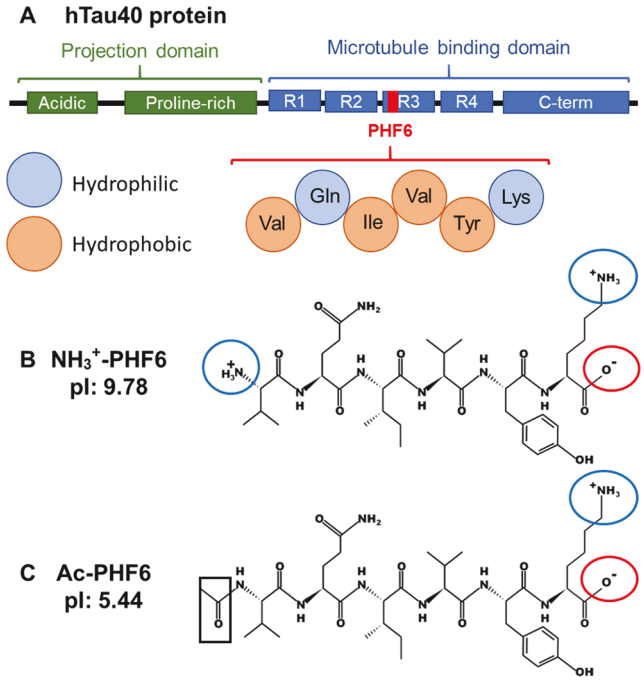

Figure 1. Structures of hTau40 protein and PHF6 peptides. *A,* hTau40, made of 441 amino acids, is the longest isoform found in the brain. It is composed of a projection domain (*green*) and microtubule-binding domain (*blue*). PHF6 is a hexapeptide found in the third repeat unit of the microtubule-binding domain (R3) and is amphiphilic. *B* and *C,* structures of NH_3^+-PHF6 and Ac-PHF6 peptides at pH 6.0. The acetyl group, the positive and negative charges are indicated in *black*, *blue*, and *red*, respectively.

were also characterized in the presence of large unilamellar vesicles (LUVs). We found that both peptides preferentially inserted into the negatively charged lipid membrane, which led to different conformational changes; NH_3^+-PHF6 inserted into the lipid membrane, whereas Ac-PHF6 formed a layer at the surface. Despite different macroscale events, both PHF6s disrupted membrane stability and underwent membrane-mediated fibrillation.

Results

PHF6 is an amphiphilic hexapeptide (32) located in the third repeat unit of the tau MTB domain (Fig. 1*A*). This hexapeptide has been shown to drive tau fibrillation by forming the core of β-sheet–rich tau aggregates (11–13). Although not physiological, the advantages of using PHF6 as a model tau peptide is that we can study the specific amino acids that drive tau fibrillation and learn about their interactions with lipid membranes. Full-length tau contains 351–441 amino acids, and it likely has additional membrane interactions. It would be difficult to isolate the impacts from the fibril-prone PHF6 sequence in the context of full-length tau. In this study, we characterized the structural changes associated with PHF6 upon interaction with lipid membranes and investigated its role in cell toxicity and peptide fibrillation. Two PHF6 isoforms were evaluated, nonacetylated PHF6 (NH_3^+-PHF6) and N-terminal acetylated PHF6 (Ac-PHF6) (Fig. 1, *B* and *C*), to investigate the influence of peptide charge on fibrillation and membrane interaction.

N-acetylation of PHF6 promotes fibrillation

PHF6 has been previously described to form fibrillar aggregates rich in parallel β-sheets (13, 14). In this study we evaluated

Downloaded from http://www.jbc.org/ at ARGONNE NATIONAL LABORATORY on January 13, 2020

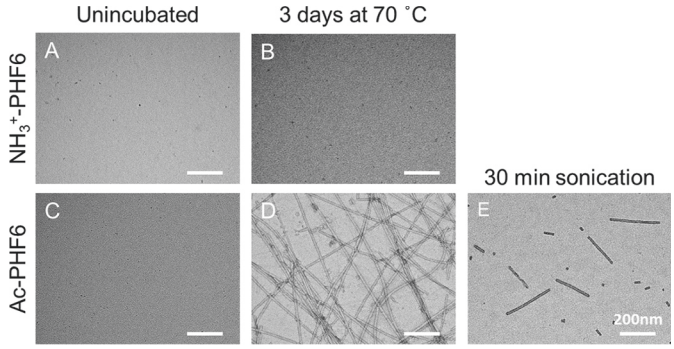

Figure 2. TEM images of NH_3^+-PHF6 and Ac-PHF6 before and after 3 days of incubation at 70 °C at 3 mg/ml under quiescent condition. Both PHF6 peptides appear monomeric when unincubated (*A* and *C*) and only Ac-PHF6 formed mature fibrils after 3 days (*B* and *D*) of incubation. Ac-PHF6 fibrils were sonicated for 30 min (*E*) to produce a mixture of short fibrils and small oligomers.

the capability of NH_3^+-PHF6 (net charge at pH 6: +1) and Ac-PHF6 (net charge at pH 6: 0) to form fibrils by incubating the peptides in MilliQ water at 3 mg/ml at 70 °C for 3 days.

As shown by TEM images in Fig. 2, *A* and *C*, unincubated NH_3^+-PHF6 and Ac-PHF6 showed very few features indicating that both peptides are soluble and likely monomeric. After 3 days of incubation at 70 °C, only Ac-PHF6 formed characteristic amyloid fibrils (Fig. 2*D*), whereas NH_3^+-PHF6 remained unaggregated (Fig. 2*B*). These results are consistent with previous findings (13) and indicate that Ac-PHF6 is more prone to fibrillation than NH_3^+-PHF6, which could be due to electrostatic repulsions between positively charged NH_3^+-PHF6 peptides. Shorter Ac-PHF6 fibrils were also produced from the long fibrils after 30 min of sonication (Fig. 2*E*). This short fibril solution was composed of smaller protofibrils with lengths in the 50–250 nm range and small globular structures with diameters around 16 nm.

PHF6 peptides are cytotoxic

We next evaluated neuronal toxicity of unincubated NH_3^+-PHF6, unincubated Ac-PHF6, and long and short Ac-PHF6 fibrils on cultured neuroblastoma SH-SY5Y cells by MTS assay. This assay is routinely used to evaluate cytotoxicity and has been previously used to evaluate toxicity of full-length tau (33). Normalized viability results are reported in Fig. 3. Compared with untreated cells (control), cells treated with unincubated and fibrillar PHF6 displayed lower levels of cell viability ($p \leq 0.01$), with final viabilities lower than the 70% threshold generally considered for cytotoxicity (34). No significant difference in cell viability was observed between cells treated with unincubated NH_3^+-PHF6 and Ac-PHF6. Additionally, both short and long Ac-PHF6 fibrils exhibited high toxicity with the short fibrils being the most cytotoxic with less than 25% viability. The higher toxicity observed for the short fibrils is supported by previous studies showing that pre-fibrillar amyloid aggregates (oligomers and protofibrils) made of full-length tau, β-amyloid, or α-synuclein display higher toxicity compared with their full-length fibril counterparts (35–38).

To complement the MTS-based cell toxicity assay, a live/dead stain assay was performed. Two stains were used, calcein-AM and ethidium homodimer-1 (EthD1). Live cells were

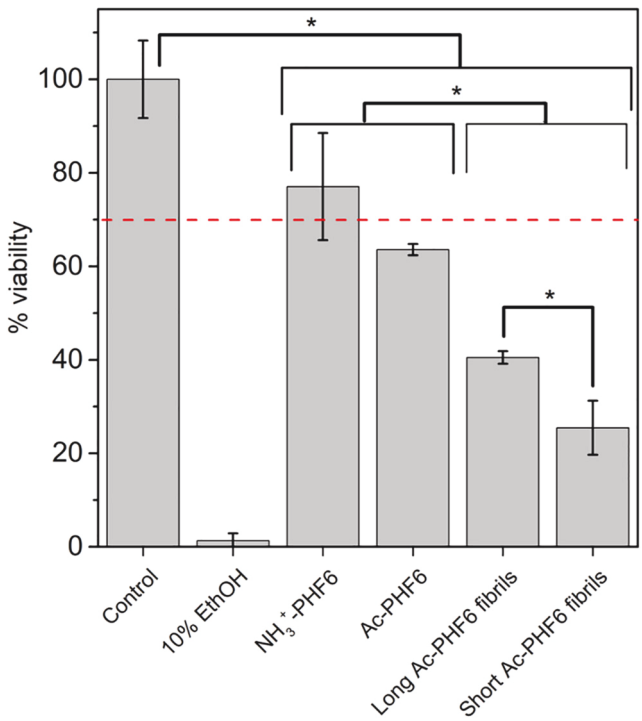

Figure 3. SHSY-5Y cell viability after 48 h of treatment with 20 μM of unincubated NH_3^+-PHF6, unincubated Ac-PHF6, pre-formed long Ac-PHF6 fibrils, and short Ac-PHF6 fibrils generated after 30 min of sonication. Cell viability was normalized to the control, untreated cells. *Error bars* represent mean ± S.D. of quintuplet experiments. *Red line* represents 70% cell viability used as a threshold for cytotoxicity. *Asterisks* indicate significant differences between two conditions (*t* test with a *p* value ≤ 0.01).

stained green by the conversion of the cell-permeant calcein-AM to green fluorescent calcein dye (excitation at 494 nm, emission at 517 nm). Membrane-compromised cells were stained red from binding of the noncell-permeant EthD1 to DNA that induces fluorescence turn-on (excitation at 528 nm, emission at 617 nm). After incubating the neuroblastoma cells with 10 μM unincubated NH_3^+-PHF6, unincubated Ac-PHF6, or fibrillar Ac-PHF6 (long and short) for 24 h, fluorescence images were taken (Fig. 4*A*) and the number of dead cells was quantified (Fig. 4*B*). Compared with the untreated control, all PHF6 samples caused significant increases in dead counts (cells/mm^2) ($p \leq 0.01$), indicating that PHF6 caused membrane permeation that could contribute to the peptide's toxicity. Comparable results were obtained for both unincubated NH_3^+-PHF6 and Ac-PHF6, indicating no significant difference in their membrane permeation activity. Additionally, the β-sheet–rich fibrils caused higher dead cell counts (Fig. 4*B*) than the unincubated peptides. Taken together, our results show that both NH_3^+-PHF6 and Ac-PHF6 are cytotoxic and the fibrillar state is more toxic and membrane disruptive compared with the unaggregated state.

PHF6 inserts into and destabilizes lipid membranes

One hypothesized mechanism of amyloid protein toxicity is the disruption of cell membrane structure and function via direct protein-membrane interactions. Indeed, the live/dead staining assay results show a correlation between PHF6 peptide toxicity and membrane permeabilization. To characterize

Downloaded from http://www.jbc.org/ at ARGONNE NATIONAL LABORATORY on January 13, 2020

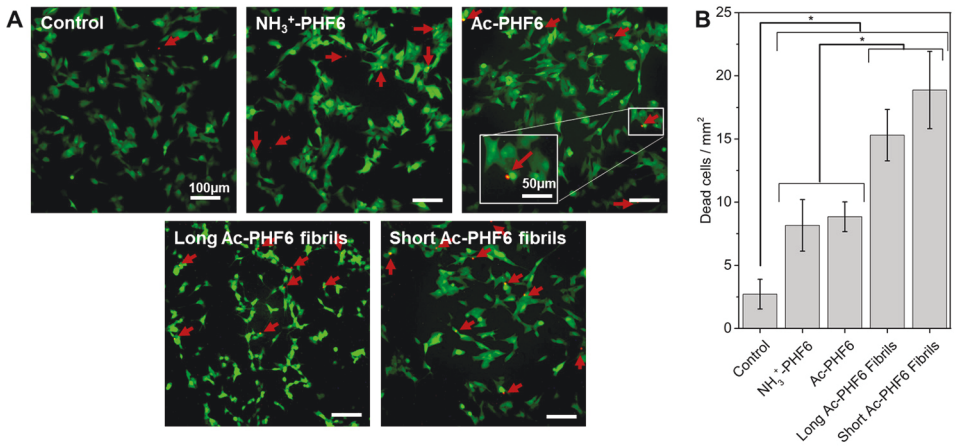

Figure 4. Live/dead staining assay results of SHSY-5Y cells incubated with 10 μM unincubated NH_3^+-PHF6, unincubated Ac-PHF6, pre-formed long Ac-PHF6 fibrils, and short Ac-PHF6 fibrils. *A,* fluorescence images of SHSY-5Y cells exposed to PHF6. *Scale bar* represents 100 μm. *Green* and *red* cells correspond to live cells (calcein-AM staining) and dead cells (EthD1 staining), respectively. The *red arrows* indicate the dead cells. A zoom-in of a dead cell is shown in the Ac-PHF6 panel where the *scale bar* represents 50 μm. *B,* quantitative results of live/dead assay images, where dead cells were counted from 4 fluorescence images taken for each treatment condition. *Asterisks* represent significant differences between two conditions (*t* test with a *p* value $\leq$ 0.01).

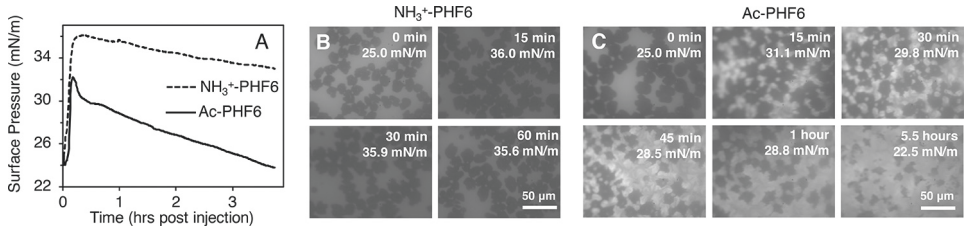

Figure 5. Isotherms (*A*) and FM images (*B* and *C*) of NH_3^+-PHF6 and Ac-PHF6 insertion into DMPG monolayer at the air/water interface under constant area conditions. 0.5 mol % fluorescent dye Texas Red-DHPE was included in the DMPG monolayer. Contrast in the FM images arises from the dye being excluded from LC domains (shown as *dark patches*), making the LE fluid lipid phase bright. Interesting, three different levels of brightness were observed in FM images of Ac-PHF6 insertion, where the LC (*dark*) and LE (*gray*) are in coexistence with a brighter phase during earlier time points (15–45 min) of Ac-PHF6 insertion.

PHF6 interactions with the cell membrane, we used lipid monolayers formed at the air/water interface in a Langmuir trough as a model membrane system. Two lipids were used, zwitterionic DMPC and anionic DMPG. The insertion of NH_3^+-PHF6 or Ac-PHF6 into monolayers was measured, whereas the monolayer surface area was held constant (Fig. 5). As such, favorable interactions that cause tau to insert into the lipid monolayer led to increases in surface pressure.

Both PHF6 peptides readily inserted into anionic DMPG monolayers, causing initial fast increases in surface pressure after injecting the peptides into the subphase (Fig. 5). Consistent with previously published findings with hTau40 (25), the truncated Ac-PHF6 did not insert into zwitterionic DMPC monolayer (data not shown), indicating that the peptide preferentially interacts with anionic lipid membranes. The insertion of NH_3^+-PHF6 resulted in higher surface pressure increases than Ac-PHF6 (Fig. 5*A*). As both peptides exhibited similar adsorption to a clean air/water interface (Fig. S1), the difference in membrane insertion was likely due to differences in their specific interactions with the lipid membrane rather than their intrinsic surface activities. After NH_3^+-PHF6 rapidly inserted into the membrane, a slow but persistent decrease in surface pressure was observed over time, indicating that some material was being removed from the surface (lipids and/or peptides). Note that this pressure loss is not due to instability of the lipid film, as lipid monolayers held at 25 mN/m did not show appreciable pressure loss over time (data not shown). Interestingly, Ac-PHF6 displayed two unique phases of surface pressure loss after the initial rapid increase: a sharp decrease in surface pressure, followed by a slower loss of about 2 mN/m per h. This two-phase surface pressure loss might be caused by different mechanisms of membrane destabilization.

To monitor lipid monolayer morphology, fluorescence microscopy (FM) was used to image the monolayer before and after peptide insertion (Fig. 5, *B* and *C*); 0.5 mol % headgroup-labeled lipid dye Texas Red DHPE (TR-DHPE) was included in the monolayer for FM imaging. A DMPG monolayer compressed to 25 mN/m has undergone phase transition where ordered liquid-condensed (LC) domains formed in the disordered liquid-expanded (LE) phase. As the bulky fluorescent dye was excluded from the LC phase, it appeared as dark patches, whereas LE phase appeared bright.

The insertion of NH_3^+-PHF6 caused negligible changes to the monolayer morphology as FM images appeared similar before and at different time points of peptide insertion (Fig. 5*B*). In contrast, insertion of Ac-PHF6 resulted in drastic changes to monolayer morphology, where at least three fluorescence intensity levels were observed in FM images (Fig. 5*C*). In addition to the bright LE and dark LC phases, a third even brighter phase was formed in the LE portion of the film at earlier time points (Fig. 5*C*, 15–45 min). These brighter features could be membrane invagination (39) caused by the insertion of Ac-PHF6. After 1 h of incubation, the third bright phase disappeared and the dark LC domains became

Downloaded from http://www.jbc.org/ at ARGONNE NATIONAL LABORATORY on January 13, 2020

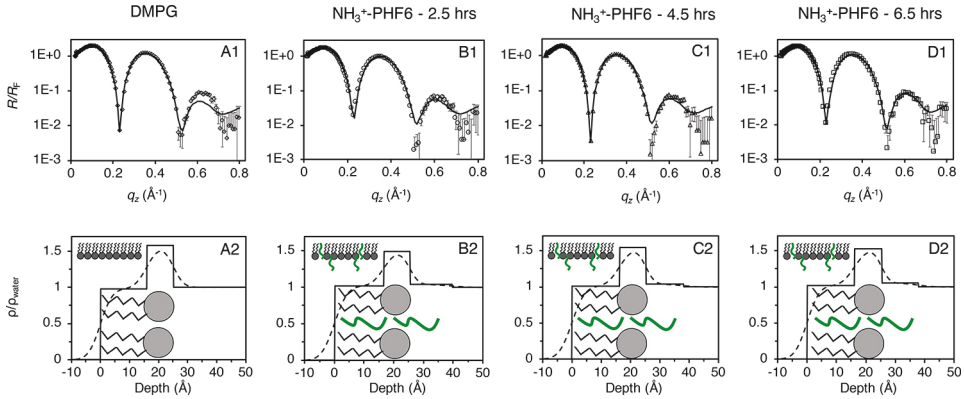

Figure 6. XR results of NH_3^+-PHF6 interacting with a DMPG monolayer. *A1–D1*, normalized Fresnel reflectivity (R/R_F) profiles of a DMPG monolayer before (*A1*) and 2.5 (*B1*), 4.5 (*C1*), and 6.5 (*D1*) h after injecting NH_3^+-PHF6 into the subphase. Experimental data are plotted as points with errors, and the fitted model is overlaid as *solid lines*. *A2–D2*, electron density profiles normalized to that of water (ρ/ρ_{water}) for a DMPG monolayer before (*A2*) and 2.5 (*B2*), 4.5 (*C2*), and 6.5 (*D2*) h after injecting NH_3^+-PHF6 into the subphase. The depth, or distance in the z-direction, is plotted with zero marking the air/lipid tails interface; negative values are in the air and positive values extend into the water subphase. *Solid lines* represent slab model fits and the *dashed lines* represent smoothed slab model fits where the slabs were fit with roughness at interfaces. Lipids and NH_3^+-PHF6 (*green*) schematics are included to help visualize the molecular layers that gave rise to the fitted ρ/ρ_{water} profiles. Larger scale schematics of the membrane structure without (*A2*) or with NH_3^+-PHF6 inserted into the membrane (*B2–D2*) are shown in the *upper left-hand corner* of the electron density profiles.

progressively reduced, which could be due to the disruption of these domains by the peptide or reduction of the monolayer surface pressure observed with time.

One cause for the higher level of insertion of NH_3^+-PHF6 compared with Ac-PHF6 could be the different overall peptide charges due to acetylation. At pH 6.0 (approximate water pH), NH_3^+-PHF6 had a net positive charge that promoted its insertion into the negatively charged lipid membrane. In contrast, Ac-PHF6 had a neutral charge and therefore had less attraction to the anionic DMPG lipid headgroups. Overall, both peptides favorably interacted with the anionic membrane and extracted material (lipids, peptides, or both) from the membrane. Additionally, our results show that although Ac-PHF6 inserted less into the membrane than NH_3^+-PHF6, it caused faster and more disruptions to the membrane stability and morphology.

NH_3^+-PHF6 inserts into the membrane while Ac-PHF6 accumulates at the membrane surface

It is clear that both PHF6 peptides destabilized the cell membrane and caused toxicity. The peptides favorably interact with anionic lipid monolayers and some differences are seen on their effects on membrane morphology. To gain further insights into the molecular level structural changes of the peptides and the lipid monolayer accompanying PHF6 insertion, we used *in situ* synchrotron X-ray scattering techniques to determine the angstrom-level structure and organization of lipids and PHF6 peptides at the air/water interface.

XR was employed to determine the electron density distribution of lipid-peptide films at the air/water interface in the direction perpendicular to the film surface (z-direction) with sub-Å resolution. Using this method one can distinguish between regions of materials with different electron densities such as, in our case, phospholipid tails, lipid headgroups, peptides, or mixtures of these components. This information can be used to reconstruct a model depicting the structure of the phospholipid/peptide film in the z-direction (averaged over the coherent volume of the X-ray beam) and determine the location of peptide in the membrane as previously described (27). A DMPG monolayer at 25 mN/m was modeled as two "slabs" of different electron densities (Fig. 6, *A1* and *A2*, and supporting Table S3), a 15.9 ± 0.2 Å thick slab of phospholipid tails at a normalized electron density (ρ/ρ_{water}) value of 0.98 ± 0.03 and a 9.1 ± 0.3 Å thick slab of more electron dense phospholipid heads with a ρ/ρ_{water} value of 1.58 ± 0.02. The insertion of NH_3^+-PHF6 into the lipid monolayer induced subtle structural changes (Fig. 6). At 2.5 h after injection, ρ/ρ_{water} of the DMPG lipid headgroups decreased from 1.58 ± 0.02 (Fig. 6, *A2*) to 1.49 ± 0.03 (DMPG + NH_3^+-PHF6) (Fig. 6, *B2*). This change could be caused by the insertion of NH_3^+-PHF6 into the lipid headgroups, thus decreasing the ρ/ρ_{water} value of this layer. The ρ/ρ_{water} values of proteins, including Aβ40 and hTau40, adsorbed to an air/water interface have been previously reported to be around 1.26 (25, 27). Thus, the intermediate ρ/ρ_{water} value of 1.49 ± 0.03 (Fig. 6, *B2*) is likely a mix of peptides and lipid headgroups. Concurrently, ρ/ρ_{water} of the lipid tails increased slightly from 0.98 ± 0.03 to 1.02 ± 0.004, suggesting some peptide insertion into the tails. A third slab was modeled beneath the lipid headgroups of electron density that was subtly distinguishable from the water subphase (ρ/ρ_{water} value of 1.041 ± 0.005). This indicated a sparsely populated layer of NH_3^+-PHF6 adsorbed to the lipid head groups. A similar observation was made at 4.5 and 6.5 h, a small change in electron density indicated NH_3^+-PHF6 insertion into the membrane and a sparse layer of adsorbed peptide.

In contrast, insertion of Ac-PHF6 induced drastic changes to the lipid monolayer structure (Fig. 7 and Table S4). After 2.5 h of Ac-PHF6 incubation with the monolayer, the membrane had clearly lost many features of its original structure. Three slabs were needed to fit the XR reflectivity data (Fig. 7, *B2*). The two slabs representing the lipid monolayer had decreased electron densities with increased roughness values indicating less distinct layers. Combined with the drastic decreases in surface pressure observed after the addition of Ac-PHF6 (Fig. 5), the decrease in electron density was likely due to loss of lipids at the surface. A third layer, extending 24.1 ± 0.07 Å into the water subphase at a ρ/ρ_{water} value of 1.21 ± 0.0014 is likely a peptide

Downloaded from http://www.jbc.org/ at ARGONNE NATIONAL LABORATORY on January 13, 2020

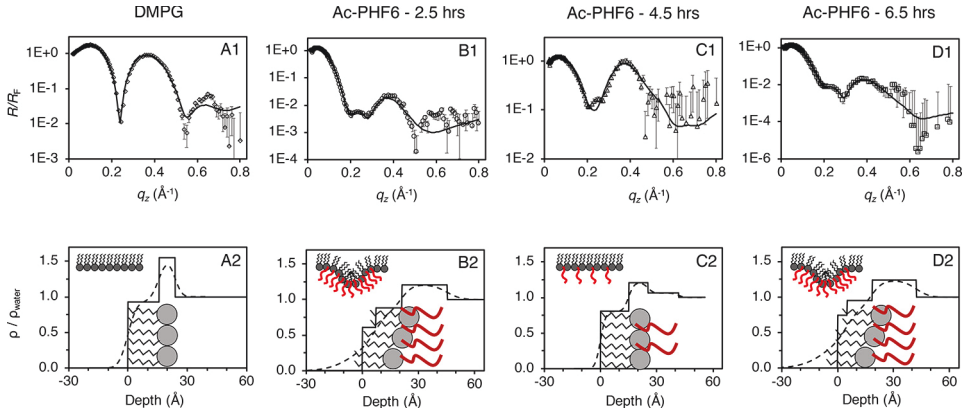

Figure 7. XR results of Ac-PHF6 interacting with a DMPG monolayer. *A1–D1*, R/R_F profiles for a DMPG monolayer before (*A1*) and 2.5 (*B1*), 4.5 (*C1*), and 6.5 (*D1*) h after injecting Ac-PHF6 into the subphase. Data are plotted as points with experiment error, and the fitted model is overlaid as *solid lines*. *A2–D2*, ρ/ρ_{water} profiles of a DMPG monolayer before (*A2*) and 2.5 (*B2*), 4.5 (*C2*), and 6.5 (*D2*) h after injecting Ac-PHF6 into the subphase. The depth is plotted with zero marking the air/lipid tails interface; negative values are in the air and positive values extend into the water subphase. The *solid lines* represent slab model fits and the *dashed lines* represent smoothed slab model fits where the slabs were fit with roughness at interfaces. Lipids and Ac-PHF6 (*red*) schematics are included to help visualize the molecular layers that gave rise to the fitted ρ/ρ_{water} profiles. Larger scale schematics of membrane structures unperturbed (*A2*) and flat (*C2*) membranes, or those containing invaginations and major deformations (*B2* and *D2*) are inlaid for each electron density profile.

Table 1
GIXD fitting parameters obtained from DMPG lipid diffraction peaks after injection of NH_3^+-PHF6 or Ac-PHF6

Sample	Surface pressure	Tail-tail intermolecular distance	Integrated peak area	Coherence length L_c[a]
	mN/m	*Å*		*Å*
NH_3^+-PHF6 lipid diffraction peaks				
DMPG	25.2	4.87 ± 0.02	668 ± 12	510 ± 80
DMPG + NH_3^+-PHF6, 1.0 h	30.0	4.96 ± 0.02	820 ± 50	120 ± 20
		4.84 ± 0.02	690 ± 20	630 ± 100
DMPG + NH_3^+-PHF6, 3.5 h	31.7	4.85 ± 0.02	277 ± 9	580 ± 90
DMPG + NH_3^+-PHF6, 5.0 h	30.8	4.84 ± 0.02	246 ± 8	600 ± 90
DMPG + NH_3^+-PHF6, 7.0 h	28.6	4.84 ± 0.02	310 ± 8	580 ± 90
Ac-PHF6 lipid diffraction peaks				
DMPG	28.9	4.870 ± 0.015	890 ± 40	480 ± 80
DMPG + Ac-PHF6, 1.0 h	37.3	4.912 ± 0.017	1200 ± 100	73 ± 11
DMPG + Ac-PHF6, 3.5 h	33.3	4.966 ± 0.018	1210 ± 60	95 ± 14
		4.841 ± 0.016	370 ± 30	340 ± 50
DMPG + Ac-PHF6, 5.0 h	30.1	4.897 ± 0.017	860 ± 60	76 ± 11
DMPG + Ac-PHF6, 7.0 h	26.3	4.91 ± 0.02	150 ± 50	90 ± 14

[a] A conservative 15% error is assumed for L_c values.

layer forming underneath the membrane (Fig. 7, *B2*). This highly perturbed monolayer structure could be the result of large-scale membrane deformations, such as invagination, which were also observed by FM imaging (Fig. 5*C*). At 4.5 h, the membrane-peptide film resembled a typical lipid monolayer with a less prominent peptide layer underneath the lipid headgroups (16.3 ± 0.3 Å thick with a ρ/ρ_{water} value of 1.06 ± 0.0018). The electron density of the lipid membrane layers decreased by about 10% compared with that at 25 mN/m, reflecting the loss of material at the surface. Finally, at 6.5 h the lipid/peptide film structure was similar to that at 2.5 h, a highly perturbed lipid monolayer covered with a thick layer of bound peptides.

PHF6 forms β-sheet–rich structures and disrupts lipid packing

Although analysis of XR data provides electron density distributions averaged over both in-plane ordered and disordered parts of the monolayer, GIXD detects only ordered diffracting species present at the air/water interface. As the expected ordered structures included condensed phospholipid tails and repeating peptide structures such as β-sheet–rich fibrillar structures, GIXD was used to monitor assembly of PHF6 peptides and its impacts on lipid packing. Fitting of integrated diffraction peaks gave rise to the lattice spacing (*d*-spacing), coherence length (L_c), and relative amounts of diffracting material in the plane of the lipid/peptide film (27). L_c is calculated from the full width at half-maximum peak intensity (FWHM) and L_c value represents the average size of diffracting crystallites. GIXD diffraction images and a summary of the peak fitting parameters are reported under supporting "Experimental procedures", Fig. S2, and Tables S1 and S2.

DMPG monolayer at 25 mN/m showed a single diffraction peak indicating hexagonally packed lipid tails in the LC phase with a distance between acyl tails of 4.87 ± 0.02 Å (Table 1) and a L_c value of 513 ± 15 Å (Table 1 and Fig. 8*A*). One hour after NH_3^+-PHF6 injection, the ordered lipid tails adopted a distorted hexagonal packing as two diffraction peaks were observed. At 3.5 h, lipid tails again became hexagonally packed. However, the total amount of diffracting lipids decreased by ~60% based on peak intensity decrease. The in-plane lipid packing remained largely the same for the rest of the experiment and no other ordered structures were observed.

In contrast, the interaction of Ac-PHF6 with DMPG was more dynamic (Fig. 8*B*, Tables 1 and 2). At 1 h after Ac-PHF6 injection, the lipid diffraction peak shifted slightly to indicate larger *d*-spacing between lipid tails. The phospholipid diffrac-

Downloaded from http://www.jbc.org/ at ARGONNE NATIONAL LABORATORY on January 13, 2020

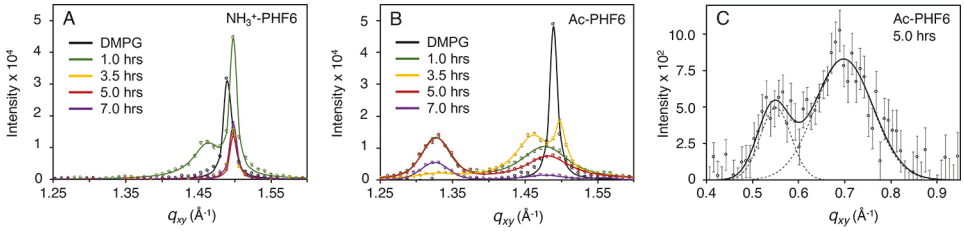

Figure 8. GIXD results of Ac-PHF6 and NH_3^+-PHF6 interacting with DMPG lipid monolayers. Background-subtracted integrated diffraction values (*points*) are overlaid with the Voigt model fit to the data (*solid lines*). *Error bars* are shown in *gray*. *A,* Bragg peaks from time-dependent NH_3^+-PHF6 interactions with a DMPG lipid monolayer. Only lipid diffraction peaks around 1.48 $Å^{-1}$ from condensed lipid tail packing were observed. *B,* Bragg peaks obtained from Ac-PHF6 interactions with a DMPG monolayer over time. The new peaks around 1.32 $Å^{-1}$ are attributed to peptide diffraction from in-registry β-sheets. *C,* GIXD peaks from Ac-PHF6 interactions with DMPG 5 h after peptide injection. No other samples showed peaks in this region.

Table 2

GIXD fit parameters of Ac-PHF6 diffraction peaks after injecting the peptide underneath a DMPG monolayer

Sample	*d*-Spacing	Integrated peak area	Coherence length L_c[a]
	Å		Å
DMPG + Ac-PHF6, 1.0 h	4.74 ± 0.02	770 ± 40	125 ± 19
DMPG + Ac-PHF6, 3.5 h	4.73 ± 0.03	150 ± 30	86 ± 13
DMPG + Ac-PHF6, 5.0 h	4.73 ± 0.03	770 ± 40	210 ± 30
	11.5 ± 0.3	43 ± 11	69 ± 10
	9.01 ± 0.14	130 ± 20	37 ± 6
DMPG + Ac-PHF6, 7.0 h	4.74 ± 0.02	280 ± 30	125 ± 19

[a] A conservative 15% error is assumed for L_c *values.*

tion peak also broadened significantly, corresponding to a more than 5-fold reduction of L_c from about 500 to 73 ± 11 Å. Concurrently, a second, nonlipid diffraction peak appeared at a q_{xy} value of 1.33 $Å^{-1}$ that corresponds to a *d*-spacing of 4.74 ± 0.02 Å (Table 2). As this *d*-spacing exactly matches the distance between β-strands of amyloid fibers previously measured by X-ray diffraction (40), the appearance of this peak indicates the formation of semi-crystalline β-strand lattice structures of Ac-PHF6 stabilized by hydrogen bonds. The L_c calculated from the peptide diffraction peak was 125 ± 19 Å, indicating that about 26 peptides are in positional registry in the crystallites. At 3.5 h, two lipid diffraction peaks were observed, indicating distorted hexagonal packing with tail-tail intermolecular distances of 4.841 ± 0.016 and 4.966 ± 0.018 Å with corresponding L_c values of 340 ± 50 and 95 ± 14 Å, respectively. Interestingly, at 3.5 h, the peptide diffraction peak diminished significantly before returning to a high intensity peak at 5 h. At 5 h the lipid diffraction indicated a return to hexagonal packing with small ordered lipid domains (L_c of 76 ± 11 Å), and at 7 h both the lipid and peptide diffraction peaks were diminished significantly.

We additionally extracted Bragg rod data by integrating X-ray diffraction images over q_{xy} to determine the length of the coherently scattering molecular entity along the *z*-dimension (L_m). Analysis of the Ac-PHF6 diffraction peak at 1.33 $Å^{-1}$ at 5 h after peptide injection yielded a L_m value of 20.2 ± 0.6 Å (Fig. S4). Thus, of the 24.12 ± 0.07-Å thick peptide layer accumulated underneath the lipid headgroups as detected by XR, 20.2 Å of it was participating in diffraction.

Taken together, GIXD resolved three distinct stages of the Ac-PHF6–membrane film after peptide addition. The first is low intensity diffraction from hexagonal lipid packing with strong peptide diffraction observed 1.0 h post-injection. At this stage, Ac-PHF6 is bound to the DMPG monolayer, and the binding disrupted lipid packing and induced the peptide to assemble in β-sheet–rich crystalline aggregates. This stage is followed by a second distinct stage of high intensity distorted hexagonal lipid packing with little peptide diffraction at 3.5 h. The interpretation of this drastic change in the peptide-lipid film is that as the β-sheet–rich Ac-PHF6 aggregates grew, they detached from the lipid monolayer and resulted in a diminished peptide diffraction peak at the air/water interface. This loss of peptides from the interface is corroborated by observed loss of surface pressure and changes in membrane morphology (Fig. 5). At this stage, another cycle of Ac-PHF6 insertion and assembly occurred (5.0–6.5 h), leading to detachment and loss of material at the interface at 7.0 h post-injection where significant surface pressure loss and only a weak lipid diffraction peak were observed.

From the GIXD data, we additionally deduced tertiary structural information about the Ac-PHF6 β-sheet–rich aggregates (or protofibrils). In GIXD the X-rays travel in the plane of the lipid monolayer and they only diffract from ordered species with their unit cell perpendicular to that plane. Thus, the β-strand unit cell must be oriented perpendicular to the lipid monolayers, which suggests that the fibril growth axis was parallel to the lipid membrane (Fig. 9*F*). At 5.0 h, two additional diffraction peaks were observed at q_{xy} values below 0.5 $Å^{-1}$ (Fig. 8*C*), with *d*-spacings of 9.0 ± 0.06 and 11.5 ± 0.13 Å. Although the exact structures that gave rise to these peaks are unknown, we posit that at least one of the peaks arose from inter-β-sheet packing of the protofibril as amyloid fibrils have been reported to have an approximate spacing of 10 Å between β-sheets (40). Thus, these diffraction peaks may have arisen from two types of inter-sheet packing arrangements. Alternatively, the diffraction could be from ordered phospholipid headgroups templated by electrostatic interactions with the protofibril. Although lipid headgroup diffraction is typically not observed by liquid surface X-ray scattering experiments, this study may be a unique case driven by the high degree of ordering in the bound protein protofibrils and their strong interaction with the negatively charged headgroups via positively charged lysine moieties. These observations, along with the XR data, corroborate dynamic Ac-PHF6–membrane interactions and structural reorganization as described previously.

With the findings from GIXD and XR, we constructed a detailed structural model for PHF6 peptide interaction with the anionic lipid membrane (Fig. 9). Favorable electrostatic interactions cause NH_3^+-PHF6 to fully insert into the phospholipid monolayer, as evidenced by modulated electron density of the headgroups and tails. A sparsely populated peptide layer was

Downloaded from http://www.jbc.org/ at ARGONNE NATIONAL LABORATORY on January 13, 2020

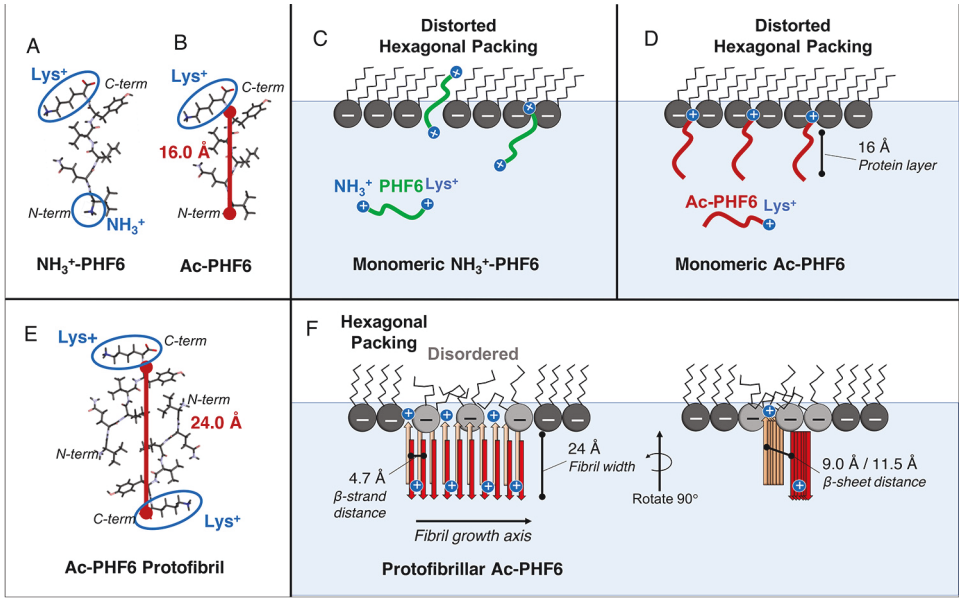

Figure 9. Model for PHF6 interactions with DMPG monolayer based on XR and GIXD data. *A*, NH_3^+-PHF6 structure extracted from a previously published structure of a paired helical filament (41). Positive charges on the peptide are *circled in blue*. *B,* Ac-PHF6 structure with the positive charge *circled in blue*. The length of the peptide (*red*) excluding the C-terminal lysine is estimated. *C,* model for nonfibrillar (unincubated) NH_3^+-PHF6 interacting with a DMPG monolayer. Electrostatic interactions drive the insertion of the positively charged peptide into the anionic DMPG monolayer. Lipid tails are in a distorted hexagonal packing structure. *D,* model for unincubated Ac-PHF6 interactions with DMPG. Peptide insets with the cationic lysine (*blue*) into the anionic DMPG headgroup. A 16-Å layer of peptide is observed below the lipid monolayer, and lipids are in a distorted hexagonal structure. *E,* model of an Ac-PHF6 fibril derived from a previously published fibril structure (Fig. S3) (41). 2 peptides are shown here. Measured distance (*red*) excludes one terminal lysine, assuming that the lysine is embedded in the DMPG headgroups. Positive charges are *circled in blue*. *F,* model for inserted and assembled Ac-PHF6 protofibril interacting with DMPG monolayer. Lipid packing is disrupted due to peptide interactions, and one terminal lysine is assumed to insert into the anionic phospholipid headgroup. The fibril forms a 24-Å layer of peptide beneath the lipids. The fibril growth axis is parallel to the plane of the lipids, and there is a lattice spacing of 4.7 Å between β-strands, and 9.0 or 11.5 Å spacing between β-sheets.

observed outside of the DMPG monolayer. As a result of peptide interaction, packing of lipid tails became distorted (Fig. 9, *A* and *C*). Ac-PHF6 first interacted with DMPG to form a 16-Å thick layer of peptides underneath the lipid headgroups and induced distorted hexagonal packing of the lipid tails (Fig. 9*D*). This layer was possibly formed by burying the C-terminal cationic lysine in the anionic headgroups, leaving 16 Å of peptide to protrude below the lipid monolayer (Fig. 9, *B* and *D*). Ac-PHF6 quickly formed β-sheet–rich protofibrillar structures after inserting into the DMPG membrane as evidenced by a β-strands *d*-spacing of 4.7 Å (Fig. 9*F*). These protofibrils are oriented with the growth axis parallel to the membrane, and likely had one terminal lysine inserted into the lipid headgroups. In addition to the β-strands *d*-spacing of 4.7 Å, two additional *d*-spacings of 9.0 and 11.5 Å were also observed between the β-sheets (Fig. 9*F*). The 24-Å thickness of the peptide layer under the monolayer was consistent with the PHF6 fibril structure (41) with one terminal lysine excluded from the measurement (Fig. 9, *E* and *F*, and Fig. S3). This model was further corroborated by Bragg rod analysis of the 5.0-h Ac-PHF6 1.328-$Å^{-1}$ diffraction peak (Fig. S4). The result was that 20.2 ± 0.6 Å of the peptide layer were contributing to the diffraction peak out of the 24-Å protein layer measured by XR studies.

PHF6 interaction with LUVs promotes fibrillation

NH_3^+-PHF6 and Ac-PHF6 displayed selective favorable interactions with anionic DMPG membrane and Ac-PHF6 was also shown to assemble into β-sheet–rich protofibrils upon interaction. To investigate the effect of this interaction on peptide fibrillation, both hexapeptides were incubated in water with 100-nm LUVs composed of 70 mol % POPC and 30 mol% POPG. Peptide secondary structures, vesicle size distribution, and formation of fibrils were evaluated using circular dichroism (CD) spectroscopy, dynamic light scattering (DLS), and TEM imaging, respectively. We did not use the popular fluorescence probe thioflavin T to track fibril formation because of its poor binding to PHF6 fibrils.

Freshly solubilized NH_3^+-PHF6 and Ac-PHF6 were rich in random coils as shown by the negative peak at around 195 nm in CD spectra (Fig. 10). After a 1-h incubation with vesicles (168 μg/ml of peptide with 688 μM lipids) at room temperature, drastic changes in secondary structure were observed for both peptides; positive and negative peaks at around 200 and 218 nm, respectively, appeared, indicating the formation of β-sheet–rich structures. A stronger CD signal was observed in the case of Ac-PHF6 showing a higher β-sheet content compared with NH_3^+-PHF6. The formation of β-sheets by Ac-PHF6 corroborates our finding from GIXD measurements (Fig. 8). However, GIXD did not detect β-sheet assembly of NH_3^+-PHF6 at the pure DMPG membrane surface. CD is a bulk solution technique, thus, the measured β-sheet content in NH_3^+-PHF6 incubated with LUVs could be from the peptide adopting a β-sheet conformation in solution, and not at the surface of the membrane. As NH_3^+-PHF6 was shown to destabilize the lipid monolayer (Fig. 5), it is likely that the peptide could adopt a β-sheet conformation when complexed with dissolved lipids. Alterna-

Downloaded from http://www.jbc.org/ at ARGONNE NATIONAL LABORATORY on January 13, 2020

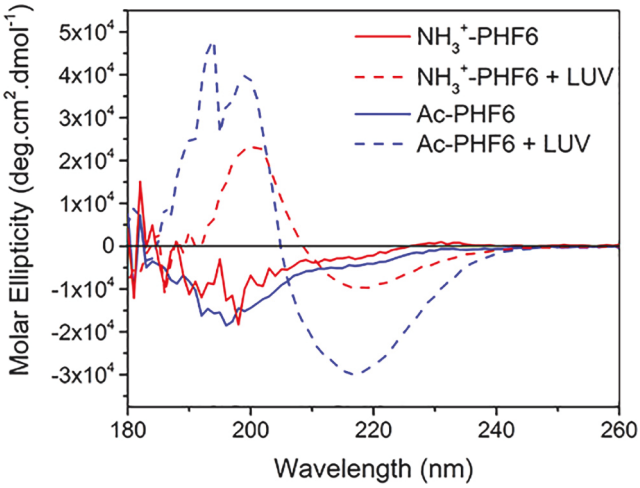

Figure 10. CD spectra of 168 μg/ml of NH_3^+-PHF6 and Ac-PHF6 peptides alone (*solid line*) and in the presence LUVs (688 μM lipids, 70 mol % POPC and 30 mol % POPG) after 1 h incubation at room temperature (*dashed line*). LUVs caused the largely random coil peptides to adopt β-sheet–rich structures.

tively, the membrane curvature found in LUVs may induce β-sheet structures more than what is observed in the flat lipid monolayer system (42, 43).

LUV size distribution was monitored by DLS during incubation with both peptides (50 μg/ml of PHF6 in the presence of 20 μM lipids) (Fig. 11). LUVs were stable for over 7 days at room temperature where the hydrodynamic radius (R_h) remained unchanged at ~50 nm (Fig. S5). The addition of NH_3^+-PHF6 to the LUVs did not induce any changes to the vesicle size distribution during the first 24 h, but the size distribution became broader and R_h increased after 6 days (Fig. 11*A*). By day 8, the vesicles likely became unstable and agglomerated. In contrast, after mixing with Ac-PHF6, an immediate broadening of LUV size distribution and increase of R_h were observed (Fig. 11*B*). By day 6, size distribution shifted toward larger sizes and became very broad. These changes are likely caused by immediate peptide binding and vesicle agglomeration, followed by peptide fibrillation at longer incubation times.

To further understand the increase of the LUV size induced by NH_3^+-PHF6 and Ac-PHF6 and the changes in secondary structures, the samples were imaged by TEM (Fig. 12). The sample containing NH_3^+-PHF6 incubated with LUVs for 1 h showed round, 100–200–nm sized features (Fig. 12*A*). These are likely peptide-coated LUVs as bare lipid vesicles are completely disrupted during the drying step in sample preparation for TEM (27). After 6 days of incubation, long fibrils were visible, which supports DLS measurements that showed the presence of larger structures in the sample. When incubated alone, NH_3^+-PHF6 did not form fibrils in the same incubation period, indicating that the interaction with the lipid membrane promoted NH_3^+-PHF6 fibrillation, possibly by reducing the repulsive electrostatic interactions between positively charge ammonium groups of NH_3^+-PHF6. Also, by binding to the lipid membrane, the increased local concentration of NH_3^+-PHF6 is also expected to promote peptide fibrillation.

In the presence of LUVs, Ac-PHF6 produced long fibrils after only a few hours of incubation (Fig. 12*B*), which is consistent with the high β-sheet content measured by CD spectroscopy (Fig. 10) and by GIXD (Fig. 8). Fibrils produced in the presence of LUVs formed large clusters connected to small dark agglomerates, which appear to be Ac-PHF6 – coated LUVs. In contrast, when the same peptide was incubated alone, significantly slower fibrillation was observed; short protofibrils were observed after 1 h and long fibrils were only observed after 6 days of incubation. Taken together, our results show that anionic vesicles accelerated fibrillation of both NH_3^+-PHF6 and Ac-PHF6.

Discussion

The interaction of the tau protein with the lipid membrane is believed to play a key role in peptide toxicity and fibrillation. In this study, we investigated the lipid membrane interaction of PHF6, a hexapeptide located in the third repeat unit of the MTB domain forming the core of tau PHFs and revealed its effect on membrane structure and peptide fibrillation. PHF6 was chosen as a model tau peptide to isolate the effect of this aggregation promoting hexapeptide motif from the full-length tau protein. We used two PHF6 peptides, one fibrillation prone (Ac-PHF6) and another not fibrillation prone (NH_3^+-PHF6), to study the effect of these peptides on cell toxicity, membrane interaction, and membrane-mediated fibrillation.

We found that both unincubated PHF6 peptides are neurotoxic and pre-formed Ac-PHF6 fibrils exert higher toxicity with the short fibrils exhibiting highest cytotoxicity (Fig. 3). Membrane disruption via direct peptide interactions has been proposed as a mode of toxicity for amyloidogenic proteins, and is the central hypothesis tested in this work. Membrane destabilization caused by PHF6 is supported by Langmuir trough isotherm experiments where both Ac-PHF6 and NH_3^+-PHF6 favorably interact with anionic, but not zwitterionic, lipid monolayers at the air/water interface (Fig. 5). This interaction leads to lipid extraction from the interface into the aqueous subphase as observed by a decrease in the membrane surface pressure after the insertion of PHF6. This model agrees with a previously published study showing that full-length tau inserts into negatively charged lipid membranes and extracts lipids (17). Furthermore, the interaction of PHF6 with lipid membranes also enhances fibrillation kinetics of both peptides. Strikingly, in the presence of anionic LUVs, Ac-PHF6 formed fibrils within 1 h of incubation, compared with 6 days required for complete fibrillation in the absence of vesicles. Likewise, the nonaggregating NH_3^+-PHF6 was able to form fibrils after 6 days of incubation with LUVs. Based on these results, we propose a 3-step model for PHF6 membrane-mediated toxicity: 1) peptide insertion into the lipid membrane, 2) membrane destabilization through lipid extraction, and 3) membrane-mediated fibrillation.

Despite a similar membrane-mediated toxicity mechanism, NH_3^+-PHF6 and Ac-PHF6 undergo different molecular level changes when interacting with the lipid membrane, which are summarized in Fig. 13. XR data (Fig. 6) indicate that the cationic NH_3^+-PHF6 fully and rapidly inserts into the negatively charged DMPG monolayer and does not immediately form β-sheets at the membrane surface but forms fibrils within 6 days (Figs. 11 and 12). Binding of the posi-

Downloaded from http://www.jbc.org/ at ARGONNE NATIONAL LABORATORY on January 13, 2020

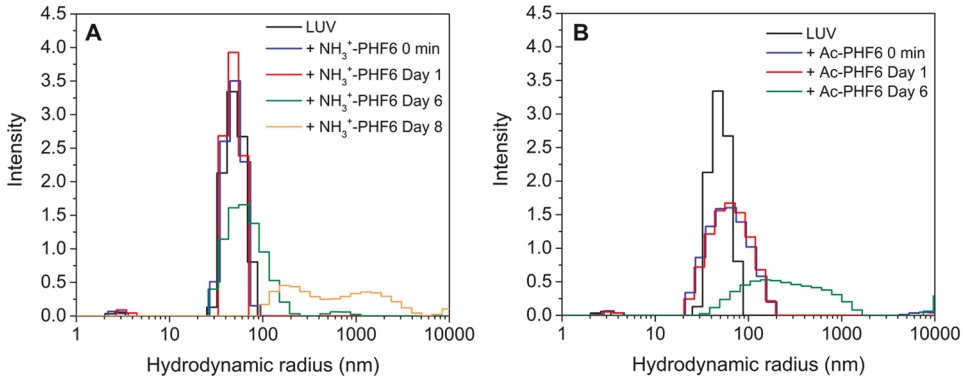

Figure 11. Size distribution of LUVs (20 μM lipids, 70 mol % POPC and 30 mol % POPG) incubated at room temperature in the presence of 50 μg/ml of NH_3^+-PHF6 (*A*) or Ac-PHF6 (*B*) over time as detected by DLS. LUVs size distribution was unchanged after 1 day of incubation with NH_3^+-PHF6 and became larger after 6 days of incubation. In contrast, Ac-PHF6 induced a rapid increase of R_h and broader LUV size distribution immediately upon addition.

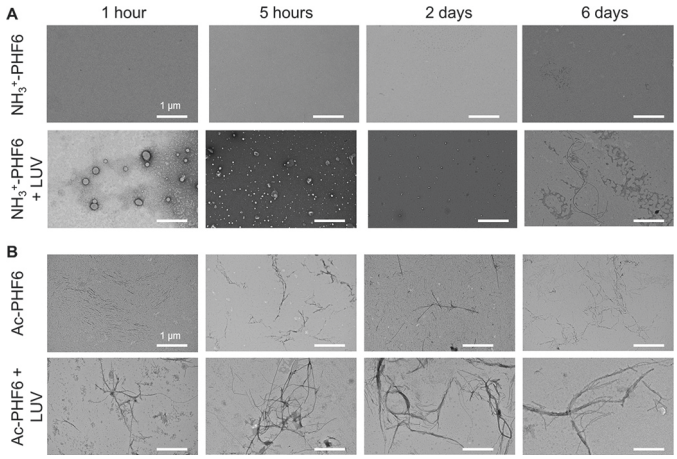

Figure 12. TEM images of NH_3^+-PHF6 (*A*) and Ac-PHF6 (*B*) incubated alone (100 μg/ml) and in the presence of LUVs (40 μM) over 6 days at room temperature under quiescent conditions.

tively charged peptides to the anionic membrane reduces the electrostatic repulsion between the peptides and increases its local concentration, both of which promote the peptide's assembly into fibrils. In contrast, Ac-PHF6 associated with the membrane, likely via lysine-mediated electrostatic interactions, but does not fully insert into the lipid headgroups (Fig. 9). The peptide quickly destabilizes the membrane (Fig. 5) and assembles into β-sheet–enriched protofibrils on the surface of the lipid membrane. These aggregates promote extensive membrane destabilization through both membrane invagination and fast peptide fibrillation.

It is important to note the difference in kinetics observed between experiments performed with a lipid monolayer made of pure DMPG lipids and LUVs made of 7:3 POPC:POPG lipids. In the LUV system, Ac-PHF6 reached complete fibrillation and disruption of the vesicles within 1 h, but in the lipid monolayer system large changes were observed up to 7 h. The differences in lipid compositions, membrane fluidity, membrane curvature, and peptide concentration are likely to influence both peptide interaction with lipid membranes and membrane destabilization kinetics, as observed in the case of α-synuclein (42). However, both of our experimental systems show the same trends for membrane interaction and fibrillation, whereas acknowledging a difference in peptide interaction kinetics.

Overall, the aggregation prone Ac-PHF6 exhibits fast membrane-mediated fibrillation and rapid membrane disruption, whereas the nonaggregation prone NH_3^+-PHF6 displays both slower membrane disruption and membrane-mediated fibrillation. Additionally, the pre-formed Ac-PHF6 fibrils displayed higher neurotoxicity than unincubated Ac-PHF6 and NH_3^+-PHF6 (Fig. 3), indicating that the peptide's assembly state and secondary structures are involved in lipid membrane destabilization and toxicity. Also, it is important to note that the lipid models used in this study were mainly composed of negatively charged lipids that do not capture the full complexity of the cell membrane. This may account for some discrepancy between the *in vitro* experiments and the *in vivo* cell toxicity assays. The cell membrane is asymmetric with a zwitterionic extracellular leaflet and anionic cytosolic leaflet (44, 45). The *in vitro* cell toxicity assay measures impacts from PHF6's interactions with the extracellular leaflet, however, they have previously been used to correlate the toxicity of full-length tau monomers, oligomers, and fibrils (33). Although the tau protein originates inside the cell, future investigations must also consider the extracellular lipid environment as it likely plays an important role in transmission of tau toxicity throughout the brain.

In this study, we have gained molecular level insights about PHF6-membrane interactions and effects of these interactions on peptide aggregation and membrane structure. With PHF6 as a model peptide for fibril-prone sequences in tau, this knowledge enhances our understanding of membrane-mediated peptide neurotoxicity and fibrillation. Our results, together with a previously published study (17), support a lipid extraction mechanism of tau-induced membrane destabilization, which results in the formation of stable peptide-lipid complexes. These complexes are also likely involved in the fast peptide fibrillation observed in the presence of vesicles. The production of such complexes could be linked to transcellular propagation as cell internalization of tau aggregates is believed to induce fibrillation of intracellular tau (10). Further study of tau-lipid complexes can shed light on the role of tau in neurodegenerative diseases and could lead to the development of novel therapeutic strategies for tau-associated neurodegenerative disorders. With this study we also introduced two PHF6 models, one fibrillation prone (Ac-PHF6) and one nonaggregation prone (NH_3^+-PHF6). These models are useful tools to study the two

Downloaded from http://www.jbc.org/ at ARGONNE NATIONAL LABORATORY on January 13, 2020

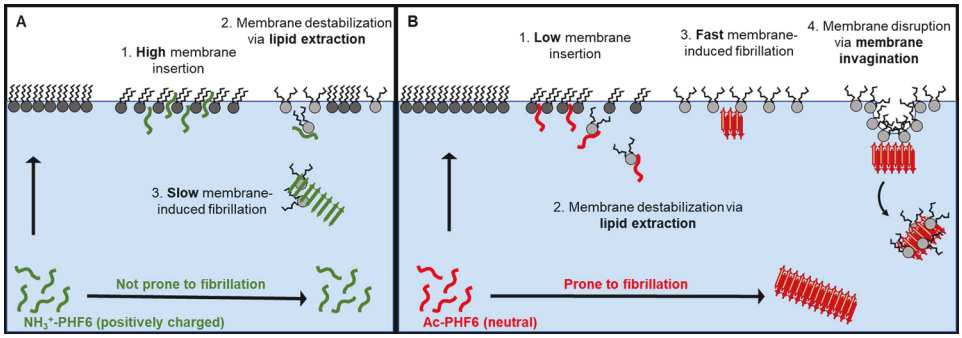

Figure 13. Model for NH_3^+-PHF6 (*A*) and Ac-PHF6 (*B*) lipid membrane disruption and membrane-induced peptide fibrillation. Nonaggregation prone NH_3^+-PHF6 quickly inserts into lipid membrane and slightly destabilizes the membrane while promoting a slow fibrillation. In contrast, the aggregation prone Ac-PHF6 rapidly inserts into lipid membrane and quickly assembles into β-sheet–rich protofibrils. Membrane destabilization and invagination occur concurrently.

toxicity events associated with amyloid proteins: membrane disruption and protein fibrillation. These PHF6 models could be used to better understand the mechanism of action of therapeutic molecules and could help elucidate the toxicity mechanisms associated with amyloid aggregates.

Experimental procedures

Materials

SH-SY5Y neuroblastoma cells, Dulbecco's modified Eagle's medium (DMEM) F-12 media, and fetal bovine serum (FBS) were purchased from Sigma. Penicillin-streptomycin (PS) at 10,000 units/ml was purchased from Thermo Fisher Scientific (Waltham, MA). The CellTiter 96® AQueous One Solution Cell Proliferation Assay, a tetrazolium compound, MTS-based metabolic assay, was purchased form Promega (Madison, WI). Ethidium homodimer-1 (EthD-1) and calcein-AM were purchased from Invitrogen (Thermo Fisher Scientific, Waltham, MA). Lipids DMPG, POPC, and POPG were obtained from Avanti Polar Lipids (Alabaster, AL). TR-DHPE was purchased from Molecular Probes Inc. Chloroform and methanol were purchased from Millipore Sigma. A MilliQ purification system (Millipore Synergy UV) was used to purify all water used. Copper grids, 400 mesh, covered by a formvar/carbon film (5–10 nm) were purchased from Ted Pella (Redding, CA) and 2% aqueous uranyl acetate was purchased from Electron Microscopy Sciences (Hatfield, PA).

Peptide synthesis, purification, and incubation

N-Acetyl-VQIVYK (Ac-PHF6) and nonacetylated VQIVYK (NH_3^+-PHF6) were synthesized by a solid-phase method as previously described (13). Peptides were purified by reverse phase-HPLC (RP-HPLC) using an acetonitrile-water gradient containing 0.1% TFA. Purified PHF6 were lyophilized and stored at −70 °C until use. Peptide molecular weights were confirmed by electrospray ionization MS and peptide purity was determined by RP-HPLC. Stock solutions were prepared by solubilizing the peptides in MilliQ water at 4 mg/ml and filtering with a 0.02-μm filter. PHF6 concentration was determined by absorbance measurement using a Nanodrop (Thermo Fisher Scientific) (ϵ280 nm = 1195.9 cm^{-1} M^{-1} (46), $MW_{Ac\text{-}PHF6}$ = 790 g/mol, $MW_{NH3+\text{-}PHF6}$ = 748 g/mol). PHF6 peptides were incubated at 70 °C for 3 days at 3 mg/ml or at room temperature for up to 6 days at 100 μg/ml to produce fibrils. Ac-PHF6 fibrils produced after 3 days of incubation at 70 °C were sonicated for 30 min with a 550T Ultrasonic Cleaner (VWR International, Radnor, PA) to form shorter fibrils.

MTS-based cell viability assay

SH-SY5Y neuroblastoma cells at passage 20 were cultivated at 37 °C and 5% CO_2 in DMEM F-12 media containing 10% FBS and 1% PS. 96-Well-plates were seeded with 20,000 cells/well. Cells were incubated for 16 h to allow cell attachment prior to serum deprivation over 24 h ensuring cell synchronization to a quiescent state. Cells were then treated with 20 μM PHF6 for 48 h. After treatment, cell viability was determined by the MTS reduction assay. The assay was performed by adding 20 μl of CellTiter 96® AQueous One Solution Cell Proliferation Assay to each well. The conversion of MTS into formazan by metabolically active cells was monitored through absorbance at 490 nm after 3 h of incubation at 37 °C and 5% CO_2. The optical density (OD) of formazan was measured using a Spectra Max M2 plate reader (Molecular Devices, Sunnyvale, CA). The % cell viability was calculated using Equation 1.

$$\%\ \text{Viability} = \frac{OD_{sample} - OD_{background}}{OD_{control} - OD_{background}} \times 100 \qquad \text{(Eq. 1)}$$

The control and background samples consisted of untreated cells and unseeded wells, respectively. Each condition was tested in quintuplet and data were statistically analyzed using JMP Pro 13 software (SAS Institute, Inc., Cary, NJ). The effect of the PHF6 on cell viability was analyzed using *t* test with a *p* value ≤ 0.01 and 70% cell viability was used as a threshold to define cytotoxicity.

Live/dead staining assay

SH-SY5Y cells were grown in a 6-well-plate at 150,000 cells/well. After 24 h incubation at 37 °C and 5% CO_2, cells were treated with 10 μM PHF6 peptide diluted in DMEM F-12 media containing 10% FBS and 1% PS. After another 24 h, cells were incubated with 1 μM EthD-1 and 0.2 μM calcein-AM in DMEM F-12 media over 30 min at 37 °C and 5% CO_2. Cells were rinsed with media and imaged using a Nikon Eclipse TS100 fluorescence microscope (Nikon Instruments, Inc., Melville, NY). Two filters blocks were used. A TRITC (G2E/C) filter cube was used to detect

Downloaded from http://www.jbc.org/ at ARGONNE NATIONAL LABORATORY on January 13, 2020

EthD-1 (red fluorescence) and a FITC (B2E/C) filter cube was used to detect calcein (green fluorescence). Images were then merged using ImageJ (National Institutes of Health, Bethesda, MD). Finally, dead cell density (number of dead cells/mm^2) was determined and the results were statistically analyzed using JMP Pro 13 software (SAS Institute, Inc., Cary, NJ) based on the average of four images taken for each condition with both filters. The effect of PHF6 on the number of dead cells/mm^2 was analyzed using t test with a p value ≤ 0.01.

Lipid monolayer insertion assays

A Langmuir trough (KSV Instruments Ltd., Finland) Micromini model with Delrin barriers was used to measure insertion of NH_3^+-PHF6 and Ac-PHF6 into a lipid monolayer composed of 100% DMPG. Water (50 ml) was used as the subphase, and experiments were performed at 30 ± 0.5 °C (temperature was controlled via a circulating water bath). DMPG was initially dissolved at 3.0 mg/ml in 7:3 (v/v) chloroform to methanol solution and sonicated. TR-DHPE was dissolved in 9:1 chloroform to methanol at 0.5 mg/ml. The final spreading solution for the trough was composed of 0.2 mg/ml of DMPG with 0.5 mol % TR-DHPE in 9:1 (v/v) chloroform to methanol. After spreading the lipids on the air/water interface, solvent was allowed to evaporate for 10 min before compressing the lipids with symmetric barriers at 3.0 mm/s to a surface pressure of 25 mN/m. For constant area experiments, the barrier position was fixed so that peptide insertion resulted in pressure increase. NH_3^+-PHF6 and Ac-PHF6 were dissolved in water at 800 μM, vortexed, and the supernatant was collected after 10 min of centrifugation at 14,000 rpm to remove insoluble peptides. Peptides were injected into the subphase to reach a final concentration of 5 μM in the trough subphase. Fluorescence microscopy images were taken with an IX51 model inverted fluorescent microscope (Olympus) and with an Exi Aqua Bio-Imaging Camera (QImaging).

X-ray scattering experiments

X-ray scattering experiments were performed at the Advanced Photon Source at Argonne National Labs, Sector 15 NSF's ChemMatCARS. Experiments were carried out in a 6.5 × 6.5 cm^2 (20-ml subphase volume) Langmuir trough equipped with a Wilhelmy plate balance. Water subphase was degassed and maintained at room temperature (~23 °C) and DMPG was deposited at the air/water interface to form a monolayer at 25 mN/m. An aliquot of NH_3^+-PHF6 or Ac-PHF6 was then injected into the subphase to a final peptide concentration of 5 μM in the trough. To prevent background scattering and oxidative beam damage to the monolayer, the trough was in a sealed canister and purged with helium gas to reduce the gaseous oxygen content to <2%. The wavelength of the X-ray beam was 1.24 Å, and X-rays were detected with a Dectris PILATUS 100K detector. Data were integrated using Python software built by beamline support scientists (https://github.com/weibu/Liquid_Surface_ChemMatCARS).[4] A typical set of XR and GIXD scans required ~45–60 min to obtain. As an additional precaution against beam damage, the trough was systematically translated during data collection. The dimensions of the incoming X-ray beam footprint on the liquid surface were ~1 mm by 3–10 mm for XR, and ~1 mm by 29 mm for GIXD. XR and GIXD measurements were collected and analyzed as described in the supporting "Experimental procedures".

Preparation of LUVs

LUVs composed of 70 mol % POPC and 30 mol % POPG were prepared as previously described (27). A 4 mM lipid solution was prepared in chloroform and dried overnight under vacuum. Dried lipid film was rehydrated with MilliQ water to 2 mM concentration. Lipid solution was vortexed and incubated for 30 min at room temperature before being exposed to five freeze/thaw cycles. Finally, rehydrated lipids were extruded 19 times using an extruder with 100 nm pore size polycarbonate membranes (Avanti Polar Lipids, Alabaster, AL).

CD spectroscopy

PHF6 secondary structures were analyzed immediately after solubilization in water at 168 μg/ml and after 1 h incubation in the presence of 688 μM LUVs by CD spectroscopy using an AVIV 410 CD spectrometer (Aviv Biomedical Inc., Lakewood, NJ). A 0.1-cm path length quartz cell (Starna Cells, Atascaders, CA) was used and CD spectra were obtained in triplicates between 180 and 260 nm with an averaging time of 15 s. The average CD signal in millidegree was then converted to molar ellipticity (θ) (47).

DLS

LUVs were analyzed by DLS to determine their size distribution when incubated alone at 20 μM or in the presence of 50 μg/ml of NH_3^+-PHF6 or Ac-PHF6. Samples were analyzed using a DAWN HELEOS II light scattering instrument (Wyatt Technology Corporation, Santa Barbara, CA) in a quartz microcuvette. Scattering intensity at 90° was recorded over 10 min and analyzed using the regularization tool on ASTRA 5.3.4.20 software.

TEM imaging

PHF6 peptides were imaged by TEM to visualize fibrillation. Peptides were diluted to 50 μg/ml with water and 4 μl of the diluted sample was loaded onto a glow discharge (30 s) copper grid. Excess sample was wicked away and the grid was stained 4 times with 2% uranyl acetate, 4 μl of stain for 3 min followed by 3 more stains of 1 min each. Between each staining step, excess of stain was wicked away. After staining, the grid was air dried and imaged using a HITACHI HT7700 transmission electron microscope (Hitachi High Technologies Corp., Tokyo, Japan).

Author contributions—A. M. F., C. M. V. Z., P. V. M., and J. M. investigation; A. M. F. and C. M. V. Z. visualization; A. M. F. and C. M. V. Z. writing-original draft; A. M. F., C. M. V. Z., J. M., and E. Y. C. writing-review and editing; E. Y. C. conceptualization; E. Y. C. funding acquisition.

[4] Please note that the JBC is not responsible for the long-term archiving and maintenance of this site or any other third party hosted site.

Downloaded from http://www.jbc.org/ at ARGONNE NATIONAL LABORATORY on January 13, 2020

Acknowledgments—X-ray scattering experiments were performed at the Advanced Photon Source at Argonne National Laboratory using NSF's ChemMatCARS Sector 15 beamline. NSF's ChemMatCARS Sector 15 is supported by the Divisions of Chemistry (CHE) and Materials Research (DMR), National Science Foundation, under Grant NSF/CHE-1834750. Use of the Advanced Photon Source, an Office of Science User Facility operated for the United StatesDepartment of Energy (DOE) Office of Science by Argonne National Laboratory, was supported by the United States DOE under contract number DE-AC02-06CH11357. We thank Dr. James Stroud and Taylor Britton who originally synthesized both NH_3^+-PHF6 and Ac-PHF6. We also express our gratitude to Dr. Erik B. Watkins for helpful discussion and review of this manuscript.

References

1. Tolnay, M., and Probst, A. (1999) Tau protein pathology in Alzheimer's disease and related disorders. *Neuropathol. Appl. Neurobiol.* **25,** 171–187 CrossRef Medline
2. Lee, G., Neve, R. L., and Kosik, K. S. (1989) The microtubule binding domain of tau protein. *Neuron* **2,** 1615–1624 CrossRef Medline
3. Buée, L., Bussière, T., Buée-Scherrer, V., Delacourte, A., and Hof, P. R. (2000) Tau protein isoforms, phosphorylation and role in neurodegenerative disorders. *Brain Res. Rev.* **33,** 95–130 CrossRef Medline
4. Amos, L. A. (2004) Microtubule structure and its stabilisation. *Org. Biomol. Chem.* **2,** 2153–2160 Medline
5. Gustke, N., Trinczek, B., Biernat, J., Mandelkow, E. M., and Mandelkow, E. (1994) Domains of tau protein and interactions with microtubules. *Biochemistry* **33,** 9511–9522 CrossRef Medline
6. Ballatore, C., Lee, V. M., and Trojanowski, J. Q. (2007) Tau-mediated neurodegeneration in Alzheimer's disease and related disorders. *Nat. Rev. Neurosci.* **8,** 663–672 CrossRef Medline
7. Mazanetz, M. P., and Fischer, P. M. (2007) Untangling tau hyperphosphorylation in drug design for neurodegenerative diseases. *Nat. Rev. Drug Discov.* **6,** 464–479 CrossRef Medline
8. Kolarova, M., García-Sierra, F., Bartos, A., Ricny, J., and Ripova, D. (2012) Structure and pathology of tau protein in Alzheimer disease. *Int. J. Alzheimer's Dis.* **2012,** 751526 CrossRef Medline
9. Ghoshal, N., García-Sierra, F., Wuu, J., Leurgans, S., Bennett, D. A., Berry, R. W., and Binder, L. I. (2002) Tau conformational changes correspond to impairments of episodic memory in mild cognitive impairment and Alzheimer's disease. *Exp. Neurol.* **177,** 475–493 CrossRef Medline
10. Kfoury, N., Holmes, B. B., Jiang, H., Holtzman, D. M., and Diamond, M. I. (2012) Trans-cellular propagation of Tau aggregation by fibrillar species. *J. Biol. Chem.* **287,** 19440–19451 CrossRef Medline
11. von Bergen, M., Friedhoff, P., Biernat, J., Heberle, J., Mandelkow, E.-M., and Mandelkow, E. (2000) Assembly of τ protein into Alzheimer paired helical filaments depends on a local sequence motif (^{306}VQIVYK^{311}) forming β structure. *Proc. Natl. Acad. Sci. U.S.A.* **97,** 5129–5134 CrossRef
12. von Bergen, M., Barghorn, S., Li, L., Marx, A., Biernat, J., Mandelkow, E.-M., and Mandelkow, E. M. (2001) Mutations of tau protein in frontotemporal dementia promote aggregation of paired helical filaments by enhancing local β-structure. *J. Biol. Chem.* **276,** 48165–48174 CrossRef Medline
13. Goux, W. J., Kopplin, L., Nguyen, A. D., Leak, K., Rutkofsky, M., Shanmuganandam, V. D., Sharma, D., Inouye, H., and Kirschner, D. A. (2004) The formation of straight and twisted filaments from short tau peptides. *J. Biol. Chem.* **279,** 26868–26875 CrossRef Medline
14. Plumley, J. A., and Dannenberg, J. J. (2011) Comparison of β-sheets of capped polyalanine with those of the Tau-amyloid structures VQIVYK and VQIINK: a density functional theory study. *J. Phys. Chem. B* **115,** 10560–10566 CrossRef Medline
15. Inouye, H., Sharma, D., Goux, W. J., and Kirschner, D. A. (2006) Structure of core domain of fibril-forming PHF/Tau fragments. *Biophys. J.* **90,** 1774–1789 CrossRef Medline
16. Crowther, R. A. (1991) Straight and paired helical filaments in Alzheimer disease have a common structural unit. *Proc. Natl. Acad. Sci. U.S.A.* **88,** 2288–2292 CrossRef
17. Ait-Bouziad, N., Lv, G., Mahul-Mellier, A.-L., Xiao, S., Zorludemir, G., Eliezer, D., Walz, T., and Lashuel, H. A. (2017) Discovery and characterization of stable and toxic Tau/phospholipid oligomeric complexes. *Nat. Commun.* **8,** 1678 CrossRef Medline
18. Georgieva, E. R., Xiao, S., Borbat. P. P., Freed, J. H., and Eliezer, D. (2014) Tau binds to lipid membrane surfaces via short amphipathic helices located in its microtubule-binding repeats. *Biophys. J.* **107,** 1441–1452 CrossRef Medline
19. Quist, A., Doudevski, I., Lin, H., Azimova, R., Ng, D., Frangione, B., Kagan, B., Ghiso, J., and Lal, R. (2005) Amyloid ion channels: a common structural link for protein-misfolding disease. *Proc. Natl. Acad. Sci. U.S.A.* **102,** 10427–10432 CrossRef Medline
20. Prangkio, P., Yusko, E. C., Sept, D., Yang, J., and Mayer, M. (2012) Multivariate analyses of amyloid-β oligomer populations indicate a connection between pore formation and cytotoxicity. *PLoS ONE* **7,** e47261 CrossRef Medline
21. Williams, T. L., and Serpell, L. C. (2011) Membrane and surface interactions of Alzheimer's Aβ peptide: insights into the mechanism of cytotoxicity. *FEBS J.* **278,** 3905–3917 CrossRef Medline
22. Pfefferkorn, C. M., Heinrich, F., Sodt, A. J., Maltsev, A. S., Pastor, R. W., and Lee, J. C. (2012) Depth of α-synuclein in a bilayer determined by fluorescence, neutron reflectometry, and computation. *Biophys. J.* **102,** 613–621 CrossRef Medline
23. Braun, A. R., Sevcsik, E., Chin, P., Rhoades, E., Tristram-Nagle, S., and Sachs, J. N. (2012) α-Synuclein induces both positive mean curvature and negative Gaussian curvature in membranes. *J. Am. Chem. Soc.* **134,** 2613–2620 CrossRef Medline
24. Ouberai, M. M., Wang, J., Swann, M. J., Galvagnion, C., Guilliams, T., Dobson, C. M., and Welland, M. E. (2013) α-Synuclein senses lipid packing defects and induces lateral expansion of lipids leading to membrane remodeling. *J. Biol. Chem.* **288,** 20883–20895 CrossRef Medline
25. Jones, E. M., Dubey, M., Camp, P. J., Vernon, B. C., Biernat, J., Mandelkow, E., Majewski, J., and Chi, E. Y. (2012) Interaction of Tau protein with model lipid membranes induces Tau structural compaction and membrane disruption. *Biochemistry* **51,** 2539–2550 CrossRef Medline
26. Elbaum-Garfinkle, S., Ramlall, T., and Rhoades, E. (2010) The role of the lipid bilayer in tau aggregation. *Biophys. J.* **98,** 2722–2730 CrossRef Medline
27. Chi, E. Y., Ege, C., Winans, A., Majewski, J., Wu, G., Kjaer, K., and Lee, K. Y. C. (2008) Lipid membrane templates the ordering and induces the fibrillogenesis of Alzheimer's disease amyloid-β peptide. *Proteins* **72,** 1–24 CrossRef
28. Zhu, M., Li, J., and Fink, A. L. (2003) The association of α-synuclein with membranes affects bilayer structure, stability, and fibril formation. *J. Biol. Chem.* **278,** 40186–40197 CrossRef Medline
29. Necula, M., Chirita, C. N., and Kuret, J. (2003) Rapid anionic micelle-mediated α-synuclein fibrillization *in vitro*. *J. Biol. Chem.* **278,** 46674–46680 CrossRef Medline
30. Gorbenko, G. P., and Kinnunen, P. K. (2006) The role of lipid–protein interactions in amyloid-type protein fibril formation. *Chem. Phys. Lipids* **141,** 72–82 CrossRef Medline
31. Barré, P., and Eliezer, D. (2006) Folding of the repeat domain of Tau upon binding to lipid surfaces. *J. Mol. Biol.* **362,** 312–326 CrossRef Medline
32. Sogawa, K., Minoura, K., In, Y., Ishida, T., Taniguchi, T., and Tomoo, K. (2014) CH–π interaction in VQIVYK sequence elucidated by NMR spectroscopy is essential for PHF formation of tau. *Biopolymers* **102,** 288–295 CrossRef Medline
33. Flach, K., Hilbrich, I., Schiffmann, A., Gärtner, U., Krüger, M., Leonhardt, M., Waschipky, H., Wick, L., Arendt, T., and Holzer, M. (2012) Tau oligomers impair artificial membrane integrity and cellular viability. *J. Biol. Chem.* **287,** 43223–43233 CrossRef Medline
34. Standardization, ISO (2009) ISO 10993–5: biological evaluation of medical devices: part 5: tests for *in vitro* cytotoxicity. ISO Geneva, Switzerland
35. Bhaskar, K., and Lamb, B. T. (2012) The role of Aβ and tau oligomers in the pathogenesis of Alzheimer's disease. in *Non-fibrillar amyloidogenic*

Downloaded from http://www.jbc.org/ at ARGONNE NATIONAL LABORATORY on January 13, 2020

ASBMB

protein assemblies-common cytotoxins underlying degenerative diseases, pp. 135–188, Springer, New York
36. Ferreira, S. T., Vieira, M. N., and De Felice, F. G. (2007) Soluble protein oligomers as emerging toxins in Alzheimer's and other amyloid diseases. *IUBMB Life* **59,** 332–345 CrossRef Medline
37. Ingelsson, M. (2016) α-Synuclein oligomers: neurotoxic molecules in Parkinson's disease and other Lewy body disorders. *Front. Neurosci.* **10,** 408 Medline
38. Stefani, M., and Dobson, C. M. (2003) Protein aggregation and aggregate toxicity: new insights into protein folding, misfolding diseases and biological evolution. *J. Mol. Med.* **81,** 678–699 CrossRef Medline
39. Lee, K. Y. C. (2008) Collapse mechanisms of Langmuir monolayers. *Annu. Rev. Phys. Chem.* **59,** 771–791 CrossRef Medline
40. Serpell, L. C. (2000) Alzheimer's amyloid fibrils: structure and assembly. *Biochim. Biophys. Acta* **1502,** 16–30 CrossRef Medline
41. Fitzpatrick, A. W., Falcon, B., He, S., Murzin, A. G., Murshudov, G., Garringer, H. J., Crowther, R. A., Ghetti, B., Goedert, M., and Scheres, S. H. (2017) Cryo-EM structures of tau filaments from Alzheimer's disease. *Nature* **547,** 185–190 CrossRef Medline
42. Middleton, E. R., and Rhoades, E. (2010) Effects of curvature and composition on α-synuclein binding to lipid vesicles. *Biophys. J.* **99,** 2279–2288 CrossRef Medline
43. Sugiura, Y., Ikeda, K., and Nakano, M. (2015) High membrane curvature enhances binding, conformational changes, and fibrillation of amyloid-β on lipid bilayer surfaces. *Langmuir* **31,** 11549–11557 CrossRef Medline
44. Zachowski, A. (1993) Phospholipids in animal eukaryotic membranes: transverse asymmetry and movement. *Biochem. J.* **294,** 1–14 CrossRef Medline
45. Nelson, D. L., and Cox, M. M. (2017) *Lehninger Principles of Biochemistry, Seventh Ed.*, W. H. Freeman and Company, New York
46. Gill, S. C., and von Hippel, P. H. (1989) Calculation of protein extinction coefficients from amino acid sequence data. *Anal. Biochem.* **182,** 319–326 CrossRef Medline
47. Kelly, S. M., Jess, T. J., and Price, N. C. (2005) How to study proteins by circular dichroism. *Biochim. Biophys. Acta* **1751,** 119–139 CrossRef Medline

Downloaded from http://www.jbc.org/ at ARGONNE NATIONAL LABORATORY on January 13, 2020

Membrane-mediated fibrillation and toxicity of the tau hexapeptide PHF6

Adeline M. Fanni, Crystal M. Vander Zanden, Paulina V. Majewska, Jaroslaw Majewski and Eva Y. Chi

J. Biol. Chem. 2019, 294:15304-15317.
doi: 10.1074/jbc.RA119.010003 originally published online August 22, 2019

Access the most updated version of this article at doi: 10.1074/jbc.RA119.010003

Alerts:
- When this article is cited
- When a correction for this article is posted

Click here to choose from all of JBC's e-mail alerts

This article cites 44 references, 11 of which can be accessed free at
http://www.jbc.org/content/294/42/15304.full.html#ref-list-1

Downloaded from http://www.jbc.org/ at ARGONNE NATIONAL LABORATORY on January 13, 2020

Supporting Information

Membrane-mediated fibrillation and toxicity of the tau hexapeptide PHF6

Adeline M. Fanni, Crystal M. Vander Zanden, Paulina V. Majewska, Jaroslaw Majewski and Eva Y. Chi

Supplemental Experimental Procedures:
X-ray scattering data analysis

Supplementary Tables:

Table S1: Complete GIXD Fit Parameters for NH_3^+-PHF6

Table S2: Complete GIXD Fit Parameters for Ac-PHF6

Table S3: NH_3^+-PHF6 XR Fit Parameters

Table S4: Ac-PHF6 XR Fit Parameters

Supplementary Figures:

Figure S1: Surface activity measurements of NH_3^+-PHF6 and Ac-PHF6. Adsorption of 3 μM PHF6 to a clean air/water interface at 30 °C

Figure S2: 2D grazing incidence X-ray diffraction plots

Figure S3: Model for PHF6 fibril structure deduced from published cryo-EM structures of Tau filaments

Figure S4: Bragg rod analysis of the protein diffraction peak centered at 1.328 $Å^{-1}$ measured for Ac-PHF6 interactions with DMPG 5 hours after protein injection

Figure S5: Size distribution of LUVs incubated at room temperature over time

Supplemental Experimental Procedures

X-ray scattering data analysis:

X-ray reflectivity (XR) was used to measure the electron density of materials deposited at the air/water interface on a Langmuir trough. X-ray scattering theory and the liquid diffractometer used here have been fully described previously(1-3) so they are only briefly summarized here. By measuring the intensity of reflected X-rays, one can deduce detailed information on the electron density distribution normal to the interface, $\rho(z)$, laterally averaged over both the ordered and disordered parts of the film. The reflectivity is defined as the ratio of reflected to incident beam intensities, in a specular geometry, as a function of the vertical momentum transfer vector $q_z = (4\pi/\lambda)\sin\theta$, where θ is the incident angle of the X-ray on the surface. Finally, the reflectivity curve can be analyzed to obtain the in-plane averaged electron density distribution normal to the interface.

The data was collected by tilting a germanium monochromator crystal to deflect the beam and change the angle of incidence on the sample. Intensities were collected over the range $0.01 < q_z < 0.8$ $Å^{-1}$, background subtracted, and normalized to incident beam flux. Data presented are divided by the Fresnel reflectivity (scattering from infinitely sharp air-water interface) (R_F) with error bars representing one standard deviation error for each data point. Division by the Fresnel reflectivity provided better visualization of the XR data.

In fitting reflectivity data, a 'slab' model was used to obtain the electron density profile normal to the interface(4). The studied system was divided into layers, or slabs, of certain thickness, constant ρ and interconnected by interfacial roughness approximated by error functions. The parameters of such model were adjusted using Motofit program(5) to obtain lowest χ^2 values and reasonable values of the parameters.

In GIXD experiments, an evanescent wave was generated by an incident beam striking the water surface at an angle corresponding to a value of momentum transfer vector in the z direction, $q_z = 0.85q_c$ where q_c = 0.02176 Å^{-1} is the critical momentum transfer vector for total external reflection from the water subphase. Diffracted intensities were recorded as a function of both $q_z = 2\pi\sin\alpha_f/\lambda$ where α_f is the out-of-plane angle of the diffracted beam, and $q_{xy} \approx 4\pi\sin(\theta_{xy}/2)/\lambda$ where θ_{xy} is the angle between the incident and diffracted beam projected onto the horizontal plane. The GIXD intensity resulting from a powder of 2-D, azimuthally disoriented, crystallites can be represented as Bragg peaks (resolved in the q_{xy} direction but integrated over the q_z) or Bragg rods (resolved in the q_z direction but integrated over the q_{xy}). The scattered signal was recorded using a 2-D Pilatus 100K PSD and slits to define a pinhole focusing geometry to yield a q_z *vs.* q_{xy} intensity distribution with a horizontal resolution of Δq_{xy} = 0.006 Å^{-1}. GIXD data were background subtracted and the Bragg peaks were fit with the Multi Peak Fit 2 function for Igor with Gaussian, Lorentzian, or Voigt profiles depending on the goodness of fit. A conservative 15 % error is assumed for the full width half maximum (FWHM) values from Voigt profile fits. The q_{xy} resolution of the ChemMatCARS liquid surface instrument of Δq_{xy} = 0.006 Å^{-1} was taken into consideration to calculate the FHHM values. The angular positions of the Bragg peaks determine the *d*-spacings, $d = 2\pi/q_{xy}^{max}$ (where the q_{xy}^{max} is the position of the maximum of the Bragg peak) for the 2D lattice. For hexagonally packed phospholipid acyl tails, intermolecular distance does not correspond directly to *d*-spacing, but is calculated from the *d*-spacing by the trigonometric relationship *intermolecular distance* = *d*-spacing / *sin*(60). From the FWHM of the peaks, coherence length L_c of the 2D crystallites, the average distance in the direction of the reciprocal lattice vector q_{xy} over which ordering extends, can be determined using Equation 2.

$$L_c = \frac{0.9\ x\ 2\pi}{\sqrt{FWHM^2 - 0.006^2}} \qquad (2)$$

For analysis, the areas of the Bragg peaks indicate the amounts of diffracting material present at the air/water interface. The intensity distribution along the Bragg rod reflects the molecular structure factor and could be analyzed to determine the length of the coherently scattering moiety, L_m, magnitude of its tilt vis-à-vis the surface normal, and the magnitude of molecular motion. The FWHM in the Bragg rod intensity distribution relates to the length of the diffracting molecular entity. The Bragg rods measured in this work were fitted with Equation 2 to calculate L_m values. Since the Bragg rods were very broad and the instrumental resolution along q_z is small (limited only by the size of the detector's pixel), Equation 2 was used without calculating intrinsic FWHM. Detailed analysis methods and theory have been previously described(1-3).

Supplementary Tables:

Table S1: Complete GIXD Fit Parameters for NH_3^+-PHF6.

Sample	q_{xy} Position ($Å^{-1}$)	FWHM	d Spacing (Å)	Inter-Molecule Distance (Å)	Integrated Peak Area	Coherence Length L_c (Å)	Surface Pressure (mN/m)
Lipid Diffraction Peaks							
DMPG	1.491 ± 0.007	0.0124 ± 0.0004	4.213 ± 0.017	4.87 ± 0.02	668 ± 12	513 ± 15	25.2
NH_3^+-PHF6 – 1.0 h	1.462 ± 0.007	0.0492 ± 0.003	4.30 ± 0.02	4.96 ± 0.02	820 ±50	115 ± 6	30.0
	1.498 ± 0.007	0.0107 ± 0.0003	4.194 ± 0.017	4.84 ± 0.02	690 ± 20	628 ± 18	
NH_3^+-PHF6 – 3.5 h	1.497 ± 0.007	0.0114 ± 0.0004	4.196 ± 0.018	4.85 ± 0.02	277 ± 9	580 ± 20	31.7
NH_3^+-PHF6 – 5.0 h	1.499 ± 0.007	0.0111 ± 0.0004	4.191 ± 0.018	4.84 ± 0.02	246 ± 8	600 ± 20	30.8
NH_3^+-PHF6 – 7.0 h	1.498 ± 0.007	0.0113 ± 0.0003	4.194 ± 0.017	4.84 ± 0.02	310 ± 8	582 ± 18	28.6

Table S2: Complete GIXD Fit Parameters for Ac-PHF6. Inter-molecule distance refers to the distance between alkyl tails in case of diffraction from DMPG lipids.

Sample	q_{xy} Position ($Å^{-1}$)	FWHM	d Spacing - Unit Cell a, b (Å)	Inter-Molecule Distance (Å)	Integrated Peak Area	Coherence Length L_c (Å)	Surface Pressure (mN/m)
Lipid Diffraction Peaks							
DMPG	1.490 ± 0.007	0.012 ± 0.002	4.218 ± 0.018	4.870 ± 0.015	890 ± 40	480 ± 80	28.9
Ac-PHF6 – 1.0 h	1.477 ± 0.007	0.077 ± 0.011	4.25 ± 0.02	4.912 ± 0.017	1200 ±100	73 ± 11	37.3
Ac-PHF6 – 3.5 h	1.461 ± 0.007	0.059 ± 0.009	4.30 ± 0.02	4.966 ± 0.018	1210 ± 60	95 ± 14	33.3
	1.499 ± 0.007	0.018 ± 0.003	4.192 ± 0.018	4.841 ± 0.016	370 ± 30	340 ± 50	
Ac-PHF6 – 5.0 h	1.481 ± 0.007	0.074 ± 0.011	4.24 ± 0.02	4.897 ± 0.017	860 ± 60	76 ± 11	30.1
Ac-PHF6 – 7.0 h	1.478 ± 0.009	0.062 ± 0.009	4.25 ± 0.03	4.910 ± 0.02	150 ± 50	90 ± 14	26.3
Ac-PHF6 β-Sheet Diffraction Peaks							
Ac-PHF6 – 1.0 h	1.327 ± 0.007	0.045 ± 0.007	4.74 ± 0.02	/	770 ± 40	125 ± 19	37.3
Ac-PHF6 – 3.5 h	1.329 ± 0.009	0.065 ± 0.010	4.73 ± 0.03	/	150 ± 30	86 ± 13	33.3
Ac-PHF6 – 5.0 h	1.328 ± 0.007	0.027 ± 0.004	4.73 ± 0.02	/	770 ± 40	210 ± 30	30.1
Ac-PHF6 – 7.0 h	1.326 ± 0.007	0.045 ± 0.007	4.74 ± 0.02	/	280 ± 30	125 ± 19	26.3
Ac-PHF6 low q_{xy} Protein Diffraction Peaks							
Ac-PHF6 – 5.0 h	0.545 ± 0.012	0.081 ± 0.012	11.5 ± 0.3	/	43 ± 11	69 ± 10	30.1
	0.697 ± 0.011	0.15 ± 0.02	9.01 ± 0.14	/	130 ± 20	37 ± 6	

*A conservative 15% error is assumed for *FWHM* and L_c values.

Table S3: NH_3^+-PHF6 XR Fit Parameters.

	Slab 1 (Tails)			Slab 2 (Heads)			Slab 3 (outside layer)			Subphase	
	Thickness	ρ / ρ_{water}	Roughness	Thickness	ρ / ρ_{water}	Roughness	Thickness	ρ / ρ_{water}	Roughness	Roughness	χ^2
DMPG	15.9 ± 0.2	0.98 ± 0.03	3.3 ± 0.3	9.1 ± 0.3	1.58 ± 0.02	3.4 ± 0.2	/	/	/	2.8 ± 0.4	7.8
PHF6 2.5 h	16.5 ± 0.3	1.019 ± 0.004	3.52 ± 0.03	8.9 ± 0.5	1.49 ± 0.03	3.2 ± 0.2	14.3 ± 1.0	1.041 ± 0.005	2.4 ± 0.2	5.0 ± 0.9	3.4
PHF6 4.5 h	16.2 ± 0.4	1.009 ± 0.005	3.52 ± 0.04	9.0 ± 0.7	1.5 ± 0.05	3.4 ± 0.3	12.9 ± 1.1	1.037 ± 0.005	2.4 ± 0.3	3.9 ± 0.8	3.4
PHF6 6.5 h	16.0 ± 0.3	1.017 ± 0.007	3.29 ± 0.06	9.3 ± 0.5	1.52 ± 0.03	3.4 ± 0.3	12.5 ± 0.7	1.052 ± 0.005	2.2 ± 0.2	3.9 ± 0.5	4.1

Table S4: Ac-PHF6 XR Fit Parameters.

	Slab 1 (Tails)			Slab 2 (Heads)			Slab 3 (outside layer)			Subphase	
	Thickness	ρ / ρ_{water}	Roughness	Thickness	ρ / ρ_{water}	Roughness	Thickness	ρ / ρ_{water}	Roughness	Roughness	χ^2
DMPG	15.7 ± 0.4	0.931 ± 0.007	3.59 ± 0.05	8.1 ± 0.6	1.55 ± 0.05	3.5 ± 0.3	/	/	/	2.8 ± 0.2	8.2
PHF6 2.5 h	7.2 ± 0.2	0.607 ± 0.005	12*	13.77 ± 0.03	0.883 ± 0.003	4.6*	24.12 ± 0.07	1.206 ± 0.001	4.5*	5.8*	12.1
PHF6 4.5 h	15.0 ± 0.1	0.805 ± 0.003	2.3*	10.3 ± 0.3	1.204 ± 0.005	2.3*	16.3 ± 0.3	1.061± 0.002	2.3*	2.3*	14.2
PHF6 6.5 h	4.7 ± 0.2	0.746 ± 0.005	13.1*	13.54 ± 0.04	0.952 ± 0.003	4.0*	23.60 ± 0.06	1.239 ± 0.001	4.2*	5.6*	11.0

*Fixed to reduce number of parameters during fitting

Supplementary Figures:

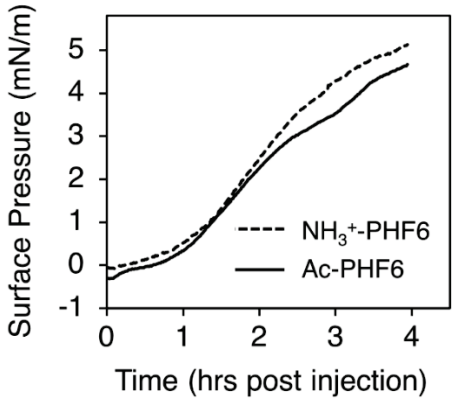

Figure S1: Surface activity measurements of NH_3^+-PHF6 and Ac-PHF6. Adsorption of 3 μM PHF6 to a clean air/water interface at 30 °C.

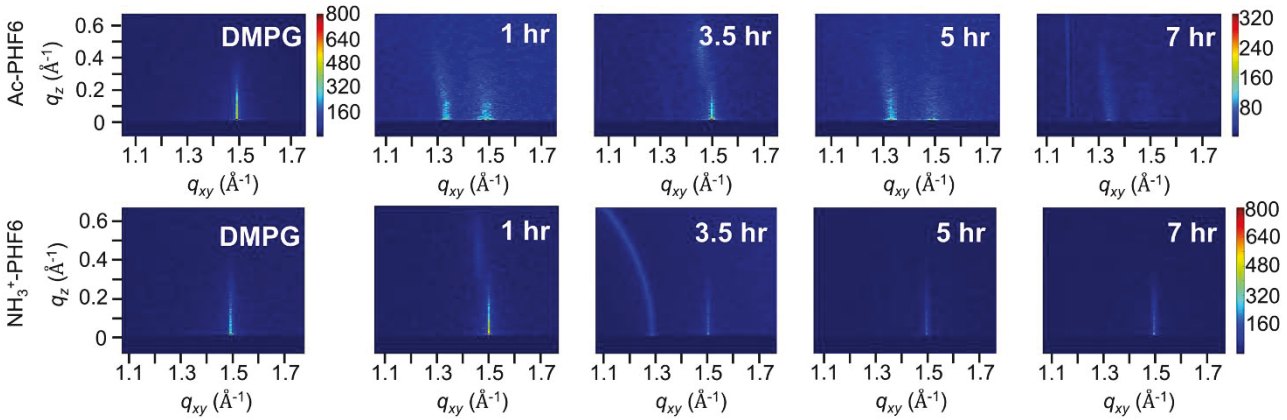

Figure S2: 2D grazing incidence X-ray diffraction plots. Raw data used for grazing incidence X-ray diffraction. Color bar on the right indicates the scale of the images, with once scale used for the top DMPG sample, another scale used for all Ac-PHF6 samples, and a third scale used for all images on the bottom (second DMPG sample and all NH_3^+-PHF6). Data collection artifacts besides the diffraction peaks are observed for Ac-PHF6 7 hours and NH_3^+-PHF6 3.5 hours. In the first case the constant line of scattering at q_{xy}=1.1 Å^{-1} was caused by an accidental vibration of the liquid surface. We believe that the scattering along Scherrer-ring observed in case of NH_3^+-PHF6 at 3.5 hours was caused by a contaminating aggregate at the surface which came into the footprint of the X-ray beam – the Langmuir trough was moved occasionally perpendicular to the x-ray beam during the scans to avoid excessive beam damage. Returning to the same position in the trough at 9 hours produced the same Scherrer-ring, thus the signal is a position-dependent contaminant and not a time-dependent scattering feature.

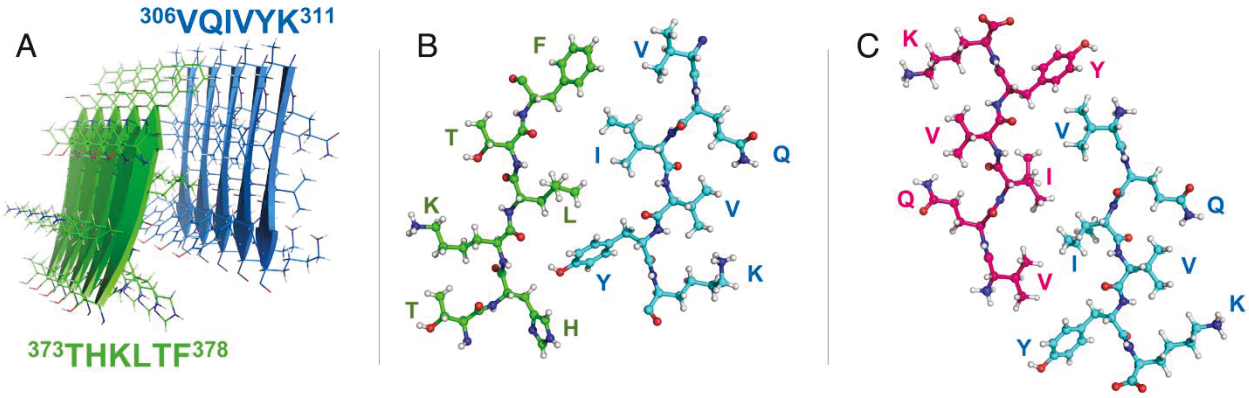

Figure S3: Model for PHF6 fibril structure deduced from published cryo-EM structures of Tau filaments**(6)**. (A) Structure of 306-VQIVYK-311 (blue) and interacting partner 373-THKLTF-378 (green) are extracted from the complete structure of a paired helical filament isolated from an Alzheimer's disease brain (PDB 5O31)(6). VQIVYK forms parallel β-sheets with cross-sheet interactions with sidechains of THKLTF. (B) Atomistic structure of 306-VQIVYK-311 (blue) interactions with 373-THKLTF-378 (green). The two peptides form a hydrophobic core of amino acid side chains to stabilize interactions cross β-sheet interactions. (C) Predicted structure for PHF6 fibrils assuming a similar cross β-sheet packing motif as the natural paired helical filament isolated from Alzheimer's brain. The original VQIVYK (blue) remains in position, while a second copy of VQIVYK (pink) was rotated and translated from the original coordinates to optimize the hydrophobic core of the structure.

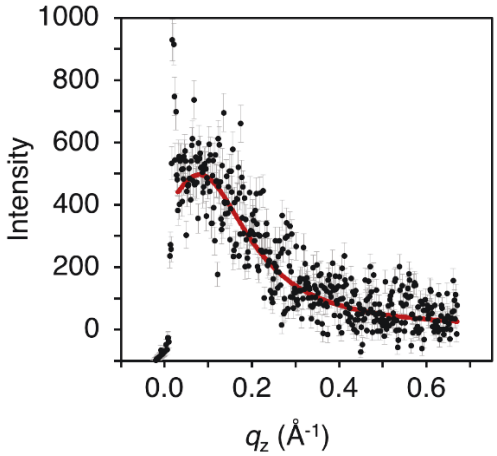

Figure S4: Bragg rod analysis of the protein diffraction peak centered at 1.328 Å^{-1} measured for Ac-PHF6 interactions with DMPG 5 hours after protein injection. Bragg rod data was extracted by integrating X-ray diffraction images along q_z for the span of the diffraction peak. Data was fit with a Lorentzian model centered around 0.08 Å^{-1} with an amplitude of 497 ± 7. The resulting FWHM from the fit was 0.277 ± 0.008 Å^{-1}, corresponding to a calculated L_m value of 20.2 ± 0.6 Å. The position of the maximum of the Bragg rod at 0.08 Å^{-1} above the horizon (defined as q_z=0 Å^{-1}) testifies that the coherently scattering molecular entity is slightly tilted from the interface normal. The sharp intensity spike at q_z~0 Å^{-1} is the Vineyard-Yoneda peak resulting from interference of the incident and refracted beams.

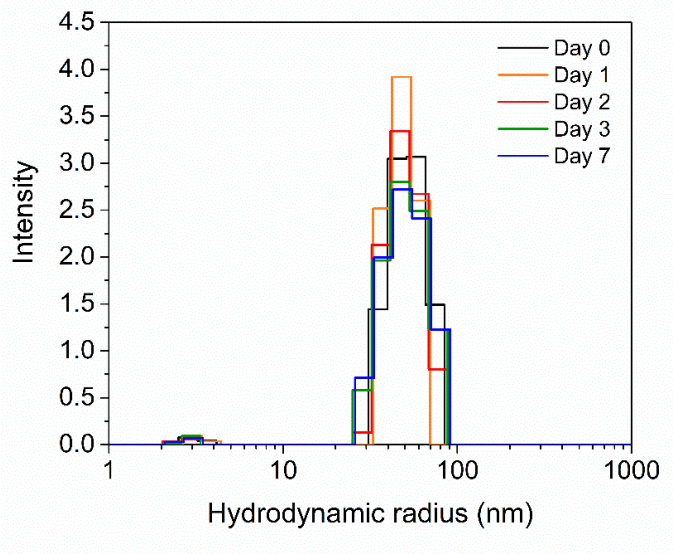

Figure S5: Size distribution of LUVs (20 µM lipids, 70%mol POPC, 30%mol POPG) incubated at room temperature over time. LUV are characterized by an overall size of 50 nm. Over 7 days of incubation at room temperature, the LUV overall size distribution was unchanged indicating high stability.

References

1. Als-Nielsen, J., and Kjaer, K. (1989) X-ray reflectivity and diffraction studies of liquid surfaces and surfactant monolayers. in *Phase Transitions in Soft Condensed Matter*, Springer. pp 113-138
2. Als-Nielsen, J., Jacquemain, D., Kjaer, K., Leveiller, F., Lahav, M., and Leiserowitz, L. (1994) Principles and applications of grazing incidence x-ray and neutron scattering from ordered molecular monolayers at the air-water interface. *Physics Reports* **246**, 251-313
3. Jensen, T. R., and Kjaer, K. (2001) Structural properties and interactions of thin films at the air-liquid interface explored by synchrotron X-ray scattering. *Novel methods to study interfacial layers* **11**, 205-254
4. Chi, E. Y., Ege, C., Winans, A., Majewski, J., Wu, G., Kjaer, K., and Lee, K. Y. C. (2008) Lipid membrane templates the ordering and induces the fibrillogenesis of Alzheimer's disease amyloid-β peptide. *Proteins: Structure, Function, and Bioinformatics* **72**, 1-24
5. Nelson, A. (2006) Co-refinement of multiple-contrast neutron/X-ray reflectivity data using MOTOFIT. *J. Appl. Crystallogr.* **39**, 273-276
6. Fitzpatrick, A. W., Falcon, B., He, S., Murzin, A. G., Murshudov, G., Garringer, H. J., Crowther, R. A., Ghetti, B., Goedert, M., and Scheres, S. H. (2017) Cryo-EM structures of tau filaments from Alzheimer's disease. *Nature* **547**, 185-190